Article

Multi-environment robotic transitions through adaptive morphogenesis

https://doi.org/10.1038/s41586-022-05188-w

Received: 21 January 2022

Accepted: 3 August 2022

Published online: 12 October 2022

Check for updates

Robert Baines[1,4], Sree Kalyan Patiballa[1,3,4], Joran Booth[1], Luis Ramirez[1], Thomas Sipple[1], Andonny Garcia[1], Frank Fish[2] & Rebecca Kramer-Bottiglio[1]✉

The current proliferation of mobile robots spans ecological monitoring, warehouse management and extreme environment exploration, to an individual consumer's home[1–4]. This expanding frontier of applications requires robots to transit multiple environments, a substantial challenge that traditional robot design strategies have not effectively addressed[5,6]. For example, biomimetic design—copying an animal's morphology, propulsion mechanism and gait—constitutes one approach, but it loses the benefits of engineered materials and mechanisms that can be exploited to surpass animal performance[7,8]. Other approaches add a unique propulsive mechanism for each environment to the same robot body, which can result in energy-inefficient designs[9–11]. Overall, predominant robot design strategies favour immutable structures and behaviours, resulting in systems incapable of specializing across environments[12,13]. Here, to achieve specialized multi-environment locomotion through terrestrial, aquatic and the in-between transition zones, we implemented 'adaptive morphogenesis', a design strategy in which adaptive robot morphology and behaviours are realized through unified structural and actuation systems. Taking inspiration from terrestrial and aquatic turtles, we built a robot that fuses traditional rigid components and soft materials to radically augment the shape of its limbs and shift its gaits for multi-environment locomotion. The interplay of gait, limb shape and the environmental medium revealed vital parameters that govern the robot's cost of transport. The results attest that adaptive morphogenesis is a powerful method to enhance the efficiency of mobile robots encountering unstructured, changing environments.

Animals that primarily inhabit one ecological niche tend to exhibit specialized body plans and gait kinematics that increase their locomotive efficiency in that niche, at the expense of degraded performance in other environments[8]. Conversely, semi-aquatic and semi-terrestrial animals display inherent morphological and gait compromises that make them only moderately efficient in both environments[12]. Environmental specialization also holds true for mobile robots, which are typically confined to operate exclusively on land or in water. The introduction of amphibious robots capable of navigating aquatic and terrestrial environments promises to advance diverse sectors such as bio-monitoring, disaster response and security[14,15], or serve as proxies to study locomotion physics in animals[16–19] (see ref. [13] for a review of amphibious robots). Importantly, amphibious robots provide pertinent platforms to evaluate design paradigms aimed at realizing efficient, multi-environment robots.

We considered that a single robot could specialize for locomotion across multi-environments through 'adaptive morphogenesis': adaptive morphology and behaviours realized through unified structural and actuation systems (see 'A note on the term 'adaptive morphogenesis'' in Methods for further discussion on this term). Towards this end, we merged specialized morphogenic features for aquatic and terrestrial locomotion—the streamlined flipper shape and gaits of sea turtles and the columnar leg shape and gaits of land-faring tortoises[20,21]—to create an Amphibious Robotic Turtle (ART) (Fig. 1a). With a single turtle-like body plan, ART employs adaptive morphogenesis through a combination of stimulus-responsive soft materials and traditional robotics components. Limbs capable of morphing between functional hydrodynamic and load-bearing shapes using variable-stiffness composites[22] (Fig. 1b, and 'Robot components and fabrication' and 'Kinematics, control and gait programming' in Methods), in tandem with a range of gaits, enable ART to swim submerged, swim at the water's surface, locomote over various substrates, and transition between land and water. Herein we study the efficacy of adaptive morphogenesis by: (1) evaluating ART's cost of transport (COT) against other animals and robots in both environments, and (2) combining favourable policies from both environments to derive transitional policies between terrestrial and aquatic habitats.

ART's body features a morphing limb able to adapt its stiffness and shape to its environment, fully integrated into a robotic structure for efficiency gain testing. The body comprises four subsystems: chassis,

[1]School of Engineering and Applied Science, Yale University, New Haven, CT, USA. [2]Department of Biology, West Chester University, West Chester, PA, USA. [3]Present address: Department of Mechanical Engineering, The University of Alabama, Tuscaloosa, AL, USA. [4]These authors contributed equally: Robert Baines, Sree Kalyan Patiballa. ✉e-mail: rebecca.kramer@yale.edu

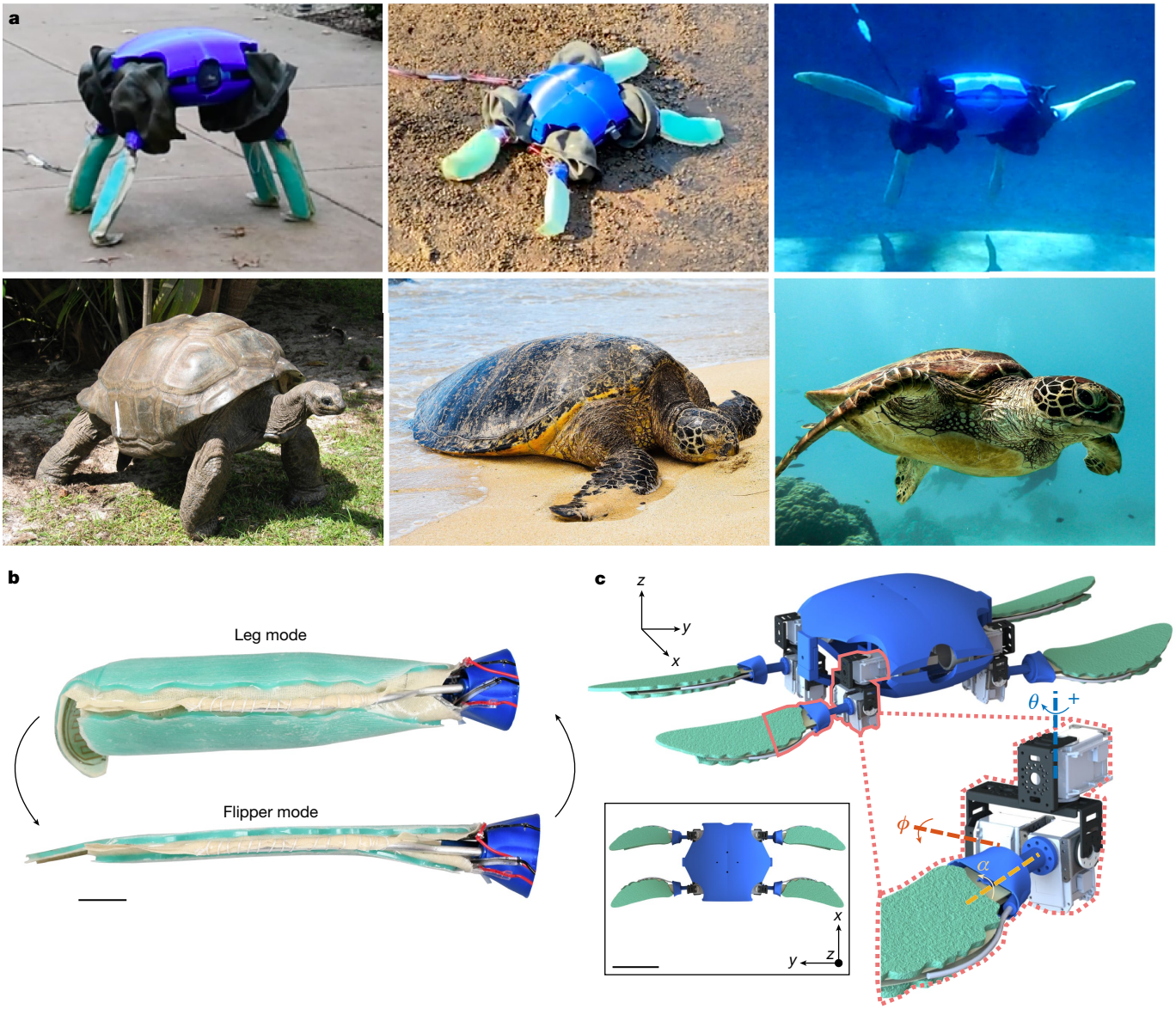

Fig. 1 | Turtle-inspired amphibious robot. a, ART replicates the limb shapes and gaits of highly adapted turtle species, and is a platform capable of specialized locomotion modes for transition between aquatic and terrestrial habitats. **b**, Side view of the morphing limb. Scale bar, 30 mm. **c**, Isometric and top views of the robot computer-aided-design model. Scale bar, 0.16 m. The inset shows the joint arrangement. The joints are typically clad in rubber bellows, removed here for visualization. θ, ϕ and α are axes for forwards and backwards, up and down, and angle-of-attack movements, respectively.

shell, shoulder joints and morphing limbs (Extended Data Fig. 1a and 'Robot components and fabrication' in Methods). The chassis holds the electronics, and the shell provides streamlining, ballast space for buoyancy tuning, payload storage and protection. The shoulder joints each have three motors in a kinematic configuration to achieve a range of gaits (Fig. 1c, Extended Data Fig. 1b and 'Kinematics, control and gait programming' in Methods). A morphing limb consisting of an antagonistic pneumatic actuator pair with strain-limiting layers adhered to thermoset polymers is connected to each shoulder joint. Heating the thermosets through embedded heaters to soften them and inflating the pneumatic actuators enables changes in limb cross-sectional area (4 times) and stiffness (storage modulus; 450 times). These changes permit ART's limbs to morph adaptively between a cylindrical geometry conducive to walking and a flat flipper geometry conducive to swimming (Supplementary Videos 4 and 5).

As ART must function in three distinct zones—water, land and the in-between transition—we calculated its COT to determine favourable limb morphology and gait pairs for each zone. COT is a dimensionless metric that allows locomotor efficiency comparisons across different robots and organisms, and is defined as: $\mathrm{COT} = P_{in}/mgv$ where m is the robot's mass, g is the acceleration due to gravity, v is the speed in the forwards direction and P_{in} is the power drawn from the motors ('Calculation of COT' in Methods).

In aquatic tests ('Swimming tests' in Methods), ART's buoyancy was adjusted for surface and submerged swimming (Fig. 2a and Supplementary Video 1). With the limbs morphed to the flipper mode, we studied paddling, as per observation of freshwater turtles and semi-aquatic mammals, and a flapping motion inspired by sea turtles and fully aquatic mammals. The paddling gait is a stroke directed ventrally rearwards relative to the robot's body, followed by a feathering recovery stroke moving forwards and dorsally. The flapping gait features a vertical movement profile of sequential upstrokes and downstrokes.

We noticed the flapping gait's strong dependence on the angle-of-attack offset $\bar{\theta}$, a constant angle deviation from ART's horizontal (0°)

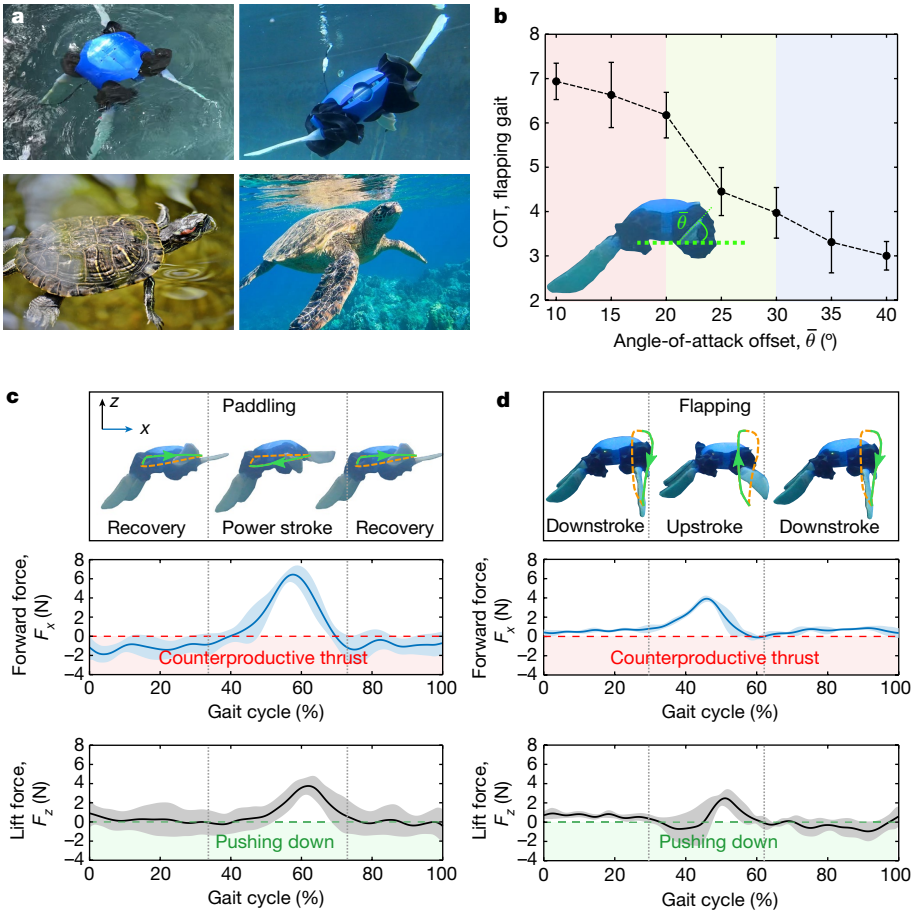

Fig. 2 | Swimming. a, The robot is capable of surface and submerged swimming by adjusting its buoyancy. **b**, Angle-of-attack offset versus COT for the sea-turtle-inspired flapping gait. Three distinct regions are highlighted: in the left (red) region, the COT of flapping was higher than that of paddling; in the middle (yellow) region, the COT drops within a span of 10°, pinpointing a transition where the robot is generating predominately productive thrust; in the right (blue) region, COT approaches its best value. The points are the average of five trials; error bars indicate one standard deviation from the mean. **c**,**d**, Snapshots of important steps over one gait cycle (top) and x (middle) and z (bottom) forces for the paddling (**c**) and flapping (**d**) gaits. The solid lines are an average of five stroke cycles and shaded regions show one standard deviation from the mean.

posture applied to the angle-of-attack motor for the duration of the stoke (Fig. 1c). A parametric study across a range of offsets pinpointed the lowest COT of 3 at $\bar{\theta} = 40°$ (Fig. 2b). Three regions were also revealed: (1) a region where flapping is less efficient than paddling owing to the generation of substantial counterproductive thrust on the downstroke; (2) a region where the COT drops (computational fluid dynamics simulations indicate that this drop coincides with a shift in the angle of attack towards more productive thrust throughout the gait cycle by reducing drag between the upstrokes and downstrokes); and (3) a region where the COT begins to plateau, suggesting that the optimal $\bar{\theta}$ for the gait is nearby (see 'Swimming tests' in Methods for more information on determining these regions).

Forward (F_x) and lift (F_z) directional forces attained by fixing ART to a multi-axis load cell elucidated the difference in the COT between paddling and the best flapping gait (Fig. 2c,d). The graph of F_x indicates counterproductive thrust is generated on the recovery portion of the paddling gait, causing ART to markedly decelerate or to move rearwards (Fig. 2c and Supplementary Video 1). Only 27% of the paddling stroke constituted productive thrust. During the downstroke of the flapping gait, ART also decelerated, but maintained productive F_x thrust for 95% of the stroke (Fig. 2d). The peak in F_z of 3.4 N during free paddling caused pitching (Supplementary Video 1). Deviation from the x direction increased ART's projected area A against oncoming flow, raising drag proportionally by $F_D = \frac{1}{2}\rho V^2 C_D A$, where V is the forward velocity, C_D is the coefficient of drag and ρ is the the density of water. In contrast, the lower peak F_z of 2.5 N during flapping maintained a more level body and nearly constant A along the flow direction.

In summary, owing to productive thrust being maintained over more of the stroke cycle and a higher sustained velocity from a reduced drag coefficient, ART's COT decreased in the favourable-angle flapping regime. The results suggest that either gait could be useful in a specific context. If high acceleration in shallow water is desired, paddling may be a viable option, but if steady, efficient swimming is favoured, flapping is the best choice. The results are consistent with the gaits of actual turtles. Paddling by freshwater turtles enhances manoeuvrability [23], whereas a flapping-style gait by sea turtles increases swimming efficiency[24]. ART exploits engineered mechanisms to accomplish both gaits while retaining the hydrodynamically favourable flipper morphology, reinforcing how adaptive morphogenesis can enable specialized robotic locomotion within an environment.

Terrestrial locomotion strategies were assessed on porcelain tile, concrete and granite—representative substrates for outdoor urban environments ('Terrestrial tests' in Methods and Supplementary Video 2). We implemented a statically stable creeping gait inspired by the upright walking of terrestrial tortoises and other quadrupedal animals for low-speed locomotion. When creeping (a lateral sequence walk), ART only has one limb off the ground at a time while incrementally pivoting its body to move forwards (Fig. 3a,b).

Three-dimensional (3D) motion capture of the distal tip of ART's back-left limb while creeping on different substrates shows a consistent

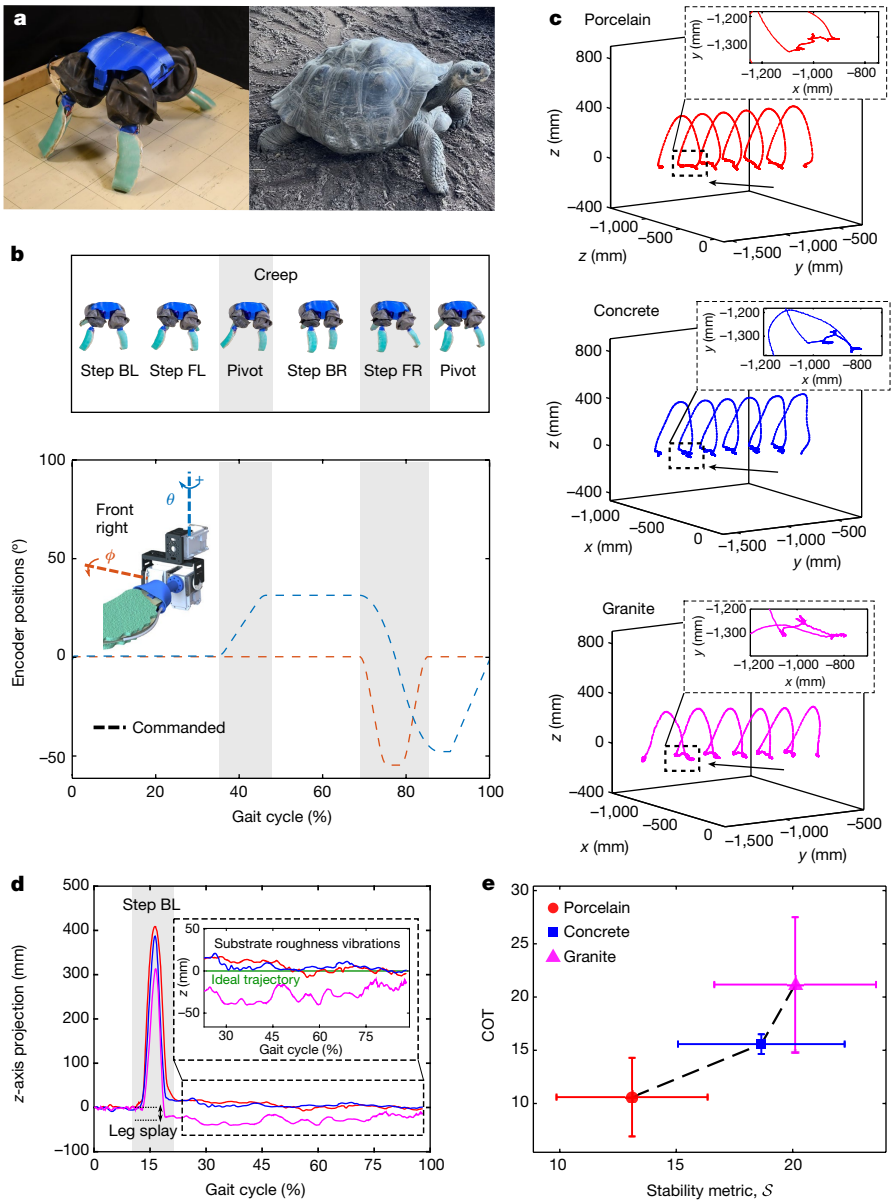

Fig. 3 | Walking. a, ART can handily traverse several terrestrial substrates with an upright creeping gait inspired by land-faring tortoises. **b**, Top: important steps over one gait cycle. Bottom: commanded encoder positions for the ϕ and θ motors. BL refers to the back left leg, BR the back right, FL the front left, and FR the front right. **c**, Three-dimensional motion capture of the distal tip of ART's back-left limb over five steps. The insets are representative projections in the x–y plane during a portion of the gait where the limb is pivoting and being used in ART's support polygon. **d**, Motion capture z-axis projection. The inset zooms to the representative pivot and stand phase used to calculate $\mathcal{S}$. **e**, The COT as a function of $\mathcal{S}$. Error bars indicate one standard deviation from the mean over five trials.

swept trajectory and stride length, verifying the efficacy of the gait (Fig. 3c and 'Terrestrial tests' in Methods). Motion capture data also help explain the COT differences across substrates. In particular, the z-axis data projection (z^*) contains (1) sharp increases when ART swings its leg for a step phase (common across all substrates), and (2) vibration signatures corresponding to interactions with the terrain, such as instabilities arising from intermittent ground contacts when in a pivot or stance phase ('Terrestrial tests' in Methods and Fig. 3d). Drift of the z-axis data over the gait cycle indicates gradual splay or tucking of the legs as ART walks.

We calculated the z-axis data's deviation from an ideal, completely stable trajectory (z) during which ART's limb would be fully in contact with the ground, as: $\mathcal{S} = \sqrt{\sum_{i=1}^{N}(z_i - z_i^*)^2}/N$ ('Terrestrial tests' in Methods). Here, $\mathcal{S}$ is the 'stability metric', denoting the extent of z-axis deviation from the ideal trajectory, and i indexes points in the trajectory from 1 to N. A positive correlation between COT and $\mathcal{S}$ underscores the importance of maintaining slip-free contact with the substrate (Fig. 3e). Substrate-dependent slippage can be attributed to friction and topographical features. For instance, the evaluated granite was coarse and exhibited a range of surface normals, which explains why its $\mathcal{S}$ was 64% higher than that of the relatively smooth porcelain.

Despite variable topographical characteristics, ART effectively traversed all evaluated substrates using a terrestrial-specialized limb geometry, illustrating the functional versatility provided through adaptive morphogenesis. ART's terrestrial locomotion abilities enable it to navigate outdoor environments with comparable facility to its swimming (Supplementary Video 2), prompting the question of what limb morphology–gait pairing will allow transitioning between land and water.

The land-to-water transition features fluidized sediment that exerts drag forces and impacts stability. Locomotor efficiency on granular

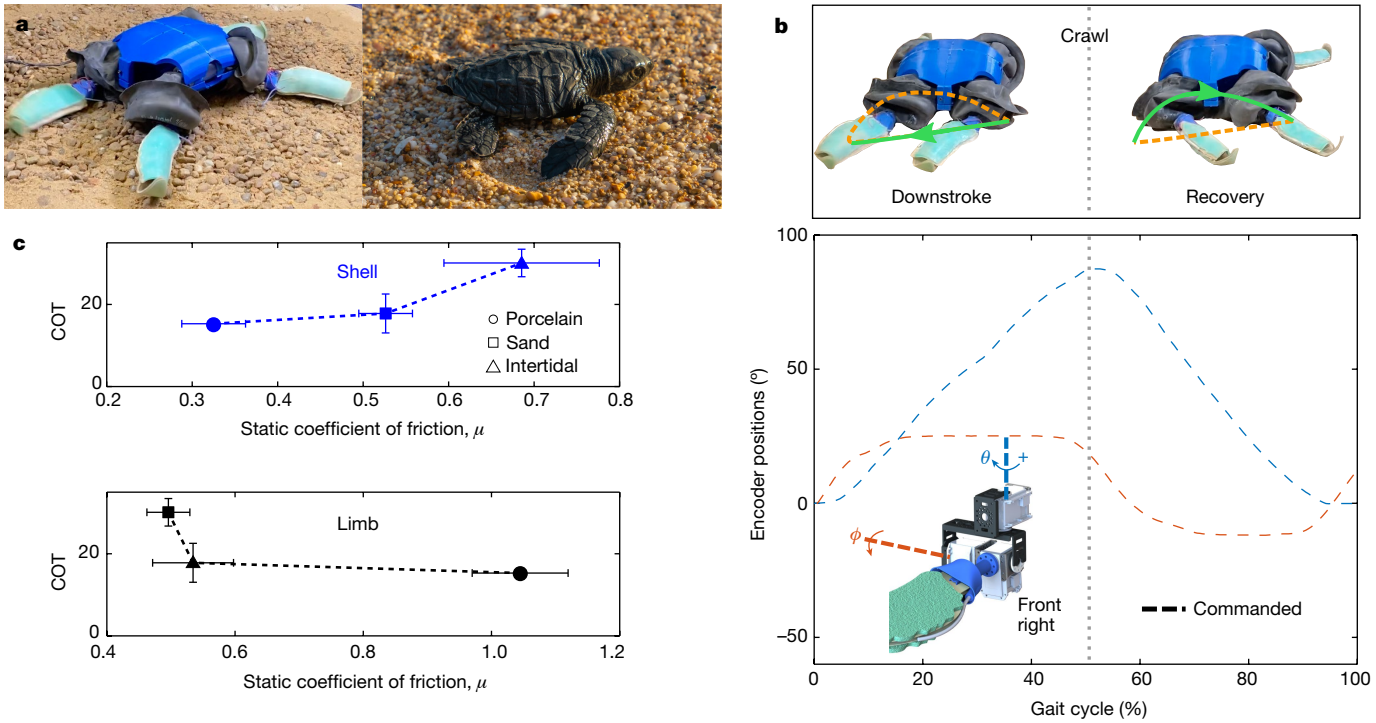

Fig. 4 | Crawling on transition substrates. a, Crawling distributes ART's weight, allowing it to traverse substrates commonly found in the transition between water and land, including sand and intertidal substrate (a mixture of sand, water and pebbles). **b**, Top: important steps over one gait cycle. Bottom: commanded encoder positions for the ϕ and θ motors. **c**, The COT plotted as a function of μ between the PLA shell (top) or elastomer limb (bottom) and the two transition substrates as well as the porcelain control surface. Horizontal error bars indicate one standard deviation from the mean over seven trials. Vertical error bars indicate one standard deviation from the mean over five trials.

media is governed by a critical yield stress dependent on substrate penetration depth[25,26], percent water content[27], and granule size and dispersity[28]. We therefore assessed locomotion strategies over representative transition terrains: dry sand and intertidal substrate—a mixture of sand, pebbles and water ('Transition-substrate tests' in Methods).

As expected, upright locomotion was unsuited to the transition substrates. In attempts to creep on sand, ART exceeded the yield stress and slipped, burrowing its limbs into the sand instead of generating forward thrust during the pivot (Supplementary Video 3). Similarly, attempts at creeping on intertidal substrate entailed slippage on the pebbles, deviating ART from its forwards trajectory. A crawling gait, akin to movements of beaching sea turtles, was selected as a means of locomotion over transition substrates. When crawling, ART lies on its belly while using both fore and aft limbs in tandem to simultaneously lift slightly upwards and push rearwards for forwards progression (Fig. 4a,b and 'Transition-substrate tests' in Methods). Crawling distributes the weight of the robot, mitigating catastrophic slip and preventing ensnarement during locomotion. By crawling, ART was able to successfully traverse both transition terrains, with 140% greater COT (averaged over all cases) than when creeping on land.

Friction tests (see 'Transition-substrate tests' in Methods for information) were conducted between the substrates and ART's constituent materials to understand the elevated COT of crawling compared with creeping. The results show a positive correlation between the COT and the static coefficient of friction (μ) for the shell and a negative correlation between the COT and μ for the limb material (Fig. 4c), suggesting that the dominant mechanics governing the COT are sliding of ART's carapace along the substrate. The grip of limbs on the substrate as well as the agglomeration of granular media at the front of the robot probably also impact the COT.

Overall, gait adaptations shifting from an upright creep to a splayed crawl permitted ART to traverse transition substrates. Although the kinematics of crawling differ substantially from those of walking, ART still uses the leg shape when crawling as it provides stiffness to push the robot upwards and forwards. This preternatural mélange of morphology and gait highlight how adaptive morphogenesis enables unprecedented ability to specialize for multiple environments.

ART's successful locomotion strategies in water, on land (Fig. 5a,b) and on transition substrate were combined to create a policy for terrestrial-to-aquatic transition (Fig. 5c). The transition site consists of an ocean inlet with hard-packed, pebbly soil flowing into a wet sandy region before becoming shallows rife with rocks and plants ('Field tests' in Methods). ART used its leg mode and creeping to traverse the hard-packed soil section. As ART approached the water and the substrate became more saturated, it started crawling, ensuring stability and preventing concentrated point loads of the upright gait from penetrating deep into the substrate. ART did not travel far into open water and lifted its limbs up out of the water before morphing ('Morphing tests' in Methods). When only partially submerged in the shallows, ART relied on paddling for swimming. ART documented its environment in-transit, causing little disruption to its surroundings (Supplementary Video 6).

ART's minimum COT performances are compared with those of a host of terrestrial and aquatic animals and robots (Fig. 5d and 'COT Comparison Chart' in Methods). ART had a minimum COT of 3 and 10 for aquatic and terrestrial locomotion, respectively. Owing to specializing for multiple environments, ART performs within the vicinity of, and in some cases outperforms, state-of-the art unimodal aquatic or terrestrial robots. For example, ART outperforms terrestrial legged robots, such as the Massachusetts Institute of Technology learning biped, by three times[29], and performs similarly to unimodal tethered quadrupeds such as Cheetah Cub and Titan V-III. ART outperforms many exclusively aquatic robots, including a dielectric elastomer actuator robotic jellyfish by ten times, and a single-motor-actuated fish by two times[30]. Crucially, ART can transition in unstructured environments while retaining comparable or better performance to unimodal robots—a feat that no robot has demonstrated so far, to our knowledge.

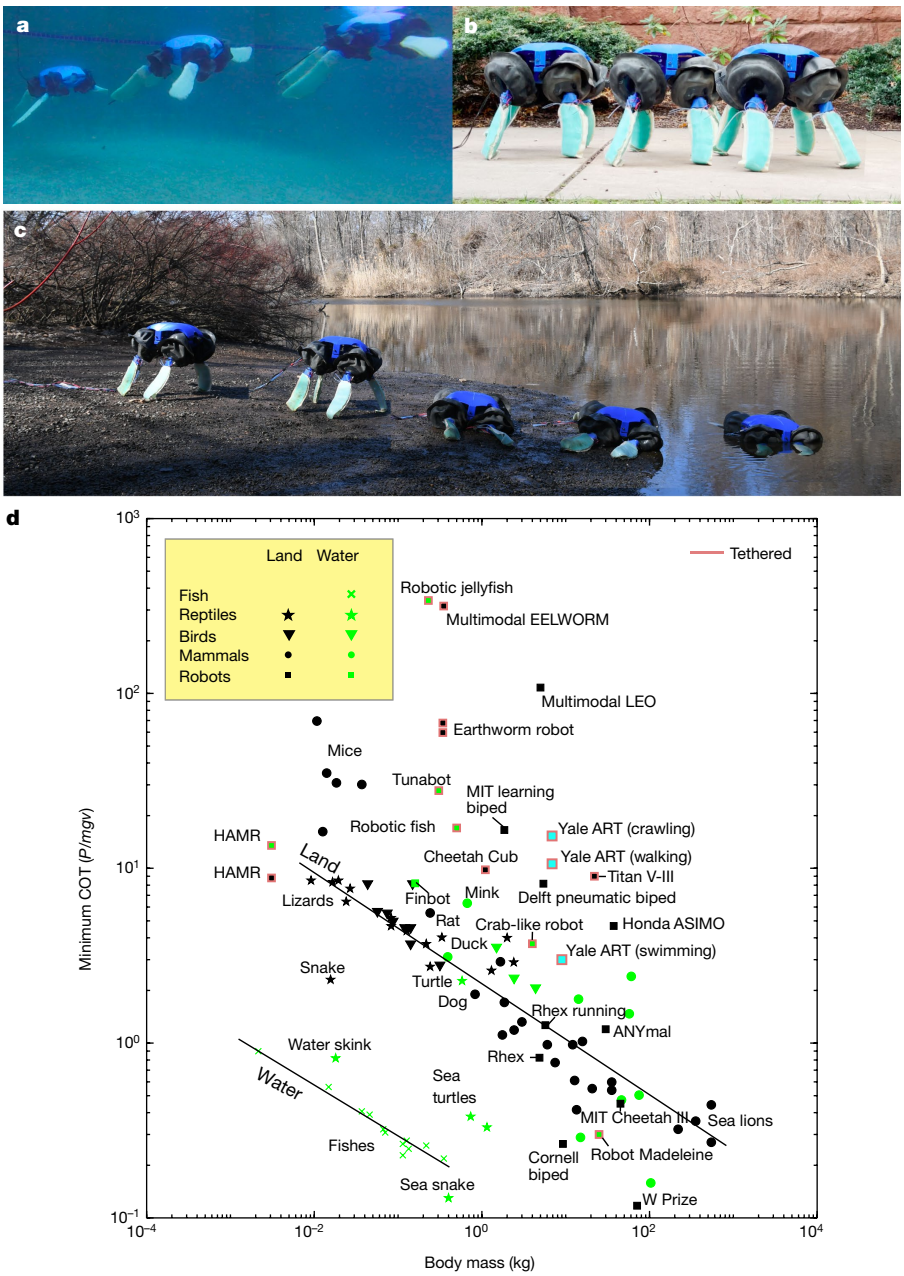

Fig. 5 | Transition policy and COT contextualization. a–**c**, Composite images with superimposed snapshots of the robot while swimming (**a**), walking (**b**) and transitioning (**c**). **d**, ART situates itself among other animals and robots well, outperforming some state-of-the-art unimodal terrestrial and aquatic robots. The robot mass increases for submerged swimming owing to incorporation of ballast. See 'Robot components and fabrication' in Methods for the references used for the plot. ASIMO refers to 'Advanced Step in Innovative MObility'; HAMR refers to 'Harvard Ambulatory MicroRobot'; LEO refers to 'LEgs ONboARD drOne' of the California Institute of Technology; MIT refers to Massachusetts Institute of Technology; and W Prize refers to a target point for legged robotic efficiency.

For unstructured, dynamic environments, such as the terrestrial-to-aquatic transition, a robot design philosophy that treats morphology and behaviour as mutable yields efficiency gains. ART combines bio-inspired aquatic, terrestrial and transitional locomotion modes through traditional robotic components, and functional shapes through variable-stiffness composites to reduce morphological and behavioural compromises. Doing so has spurred several questions, such as when and where should transitions take place, can environmental perturbations in transition be harnessed to enhance efficiency, and how close to optimal are the gaits studied herein. Beyond providing a platform to answer future questions such as these, we anticipate that the concept of uniting stimulus-responsive materials with traditional robotics components will catalyse the next generation of adaptive robotic systems.

Online content

Any methods, additional references, Nature Research reporting summaries, source data, extended data, supplementary information, acknowledgements, peer review information; details of author contributions and competing interests; and statements of data and code availability are available at https://doi.org/10.1038/s41586-022-05188-w.

1. Miki, T. et al. Learning robust perceptive locomotion for quadrupedal robots in the wild. *Sci. Robot.* **7**, eabk2822 (2022).
2. Sinatra, N. R. et al. Ultragentle manipulation of delicate structures using a soft robotic gripper. *Sci. Robot.* **4**, eaax5425 (2019).
3. D'Andrea, R. Guest Editorial: A revolution in the warehouse: a retrospective on Kiva Systems and the grand challenges ahead. *IEEE Trans. Autom. Sci. Eng.* **9**, 638–639 (2012).
4. Forlizzi, J. & DiSalvo, C. Service robots in the domestic environment: a study of the Roomba vacuum in the home. In *HRI '06: Proc. 1st ACM SIGCHI/SIGART Conference on Human–Robot Interaction* 258–265 (ACM, 2006).
5. Shah, D. et al. Shape changing robots: bioinspiration, simulation, and physical realization. *Adv. Mater.* **33**, 2002882 (2021).
6. Nygaard, T. F., Martin, C. P., Torresen, J., Glette, K. & Howard, D. Real-world embodied AI through a morphologically adaptive quadruped robot. *Nat. Mach. Intell.* **3**, 410–419 (2021).
7. Ijspeert, A. J., Crespi, A., Ryczko, D. & Cabelguen, J.-M. From swimming to walking with a salamander robot driven by a spinal cord model. *Science* **315**, 1416–1420 (2007).
8. Fish, F. E. Advantages of aquatic animals as models for bio-inspired drones over present AUV technology. *Bioinspir. Biomim.* **15**, 025001 (2019).
9. Yu, J. et al. On a bio-inspired amphibious robot capable of multimodal motion. *IEEE/ASME Trans. Mechatron.* **17**, 847–856 (2012).
10. Yu, J., Ding, R., Yang, Q., Tan, M. & Zhang, J. Amphibious pattern design of a robotic fish with wheel-propeller-fin mechanisms: amphibious pattern design of a robotic fish. *J. Field Robot.* **30**, 702–716 (2013).
11. Boxerbaum, A. S. et al. Design, simulation, fabrication and testing of a bio-inspired amphibious robot with multiple modes of mobility. *J. Robot. Mechatronics* **24**, 629–641 (2012).
12. Lock, R. J., Burgess, S. C. & Vaidyanathan, R. Multi-modal locomotion: from animal to application. *Bioinspir. Biomim.* **9**, 011001 (2013).
13. Baines, R., Fish, F. & Kramer-Bottiglio, R. in *Bioinspired Sensing, Actuation, and Control in Underwater Soft Robotic Systems* (eds Paley, D. A. & Wereley, N. M.) Ch. 2 (Springer Nature, 2021).
14. Dudek, G. et al. AQUA: an amphibious autonomous robot. *Computer* **40**, 46–53 (2007).
15. Ijspeert, A. J. Amphibious and sprawling locomotion: from biology to robotics and back. *Annu. Rev. Control Robot. Auton. Syst.* **3**, 091919–095731 (2020).
16. Nyakatura, J. A. et al. Reverse-engineering the locomotion of a stem amniote. *Nature* **565**, 351–355 (2019).
17. Mazouchova, N., Umbanhowar, P. B. & Goldman, D. I. Flipper-driven terrestrial locomotion of a sea turtle-inspired robot. *Bioinspir. Biomim.* **8**, 026007 (2013).
18. Crespi, A., Karakasiliotis, K., Guignard, A. & Ijspeert, A. J. Salamandra Robotica II: an amphibious robot to study salamander-like swimming and walking gaits. *IEEE Trans. Robot.* **29**, 308–320 (2013).
19. Ijspeert, A. J. Biorobotics: using robots to emulate and investigate agile locomotion. *Science* **346**, 196–203 (2014).
20. Wyneken, J. in *The Biology of Sea Turtles* Vol. 1 (eds Lutz, P. L. & Musick, J. A.) Ch. 7 (CRC, 1997).
21. Zani, P. A., Gottschall, J. S. & Kram, R. Giant Galapagos tortoises walk without inverted pendulum mechanical-energy exchange. *J. Exp. Biol.* **208**, 1489–1494 (2005).
22. Baines, R., Freeman, S., Fish, F. & Kramer-Bottiglio, R. Variable stiffness morphing limb for amphibious legged robots inspired by chelonian environmental adaptations. *Bioinspir. Biomim.* **15**, 025002 (2020).
23. Blob, R., Mayerl, C., Rivera, A., Rivera, G. & Young, V. On the fence versus all in: insights from turtles for the evolution of aquatic locomotor specializations and habitat transitions in tetrapod vertebrates. *Integr. Comp. Biol.* **56**, 1310–1322 (2016).
24. Rivera, A. R. V., Wyneken, J. & Blob, R. W. Forelimb kinematics and motor patterns of swimming loggerhead sea turtles (*Caretta caretta*): are motor patterns conserved in the evolution of new locomotor strategies? *J. Exp. Biol.* **214**, 3314–3323 (2011).
25. Li, C., Umbanhowar, P. B., Komsuoglu, H., Koditschek, D. E. & Goldman, D. I. Sensitive dependence of the motion of a legged robot on granular media. *Proc. Natl Acad. Sci. USA* **106**, 3029–3034 (2009).
26. Mazouchova, N., Gravish, N., Savu, A. & Goldman, D. I. Utilization of granular solidification during terrestrial locomotion of hatchling sea turtles. *Biol. Lett.* **6**, 398–401 (2010).
27. Richefeu, V., El Youssoufi, M. S. & Radjai, F. Shear strength properties of wet granular materials. *Phys. Rev. E* **73**, 051304 (2006).
28. Simoni, A. & Houlsby, G. T. The direct shear strength and dilatancy of sand and gravel mixtures. *Geotech. Geol. Eng.* **24**, 523–549 (2006).
29. Kuo, A. D. Choosing your steps carefully. *IEEE Robot. Autom Mag.* **14**, 18–29 (2007).
30. White, C. H., Lauder, G. V. & Bart-Smith, H. Tunabot Flex: a tuna-inspired robot with body flexibility improves high-performance swimming. *Bioinspir. Biomim.* **16**, 026019 (2021).

Methods

A note on the term 'adaptive morphogenesis'

We introduce the design paradigm of 'adaptive morphogenesis' to describe adaptive robot morphology and behaviours realized through unified structural and actuation systems. Our specific illustration of this design paradigm leverages a combination of soft stimulus-responsive materials and traditional robotics components to achieve on-demand changes in a quadrupedal robot's limb shape and gaits. In the term adaptive morphogenesis, 'morphogenesis' alludes to the emergence of form, and thereby function (that is, in our case, the disparate tortoise leg or turtle flipper morphology) as a result of environmental pressures[31]. 'Adaptive' refers to morphogenic features that are not fixed as they are in animals through genetic encoding; they are mutable at a condensed timescale and responsive to environmental context.

Some previous use of 'adaptive morphogenesis' in the biological literature merits mention. Specifically, in literature concerning bacteria, terms such as adaptive morphogenesis, morphological plasticity and phenotypic plasticity describe hypotheses of how bacteria change shape and size based on environmental influences[32,33]. The biological use of adaptive morphogenesis, despite being a lens through which to explain cellular-level phenomenon, relates to the same notions that we implement intentionally with our design paradigm.

Robot components and fabrication

With ballast for submerged swimming, ART's total mass is 9 kg and its density is slightly less than that of water. It spans 0.32 m from front to back, 0.96 m from limb tip to limb tip (with limbs raised up horizontally on either side) and 0.358 m width-wise (with limbs lowered to their full extent, measured about the top half of the shell). The robot comprises four distinct subsystems: polyvinyl chloride (PVC) chassis, shell, shoulder joints and limbs. The inside of the chassis and shoulder joints are hermetically sealed together as a single volume. Extended Data Fig. 1a shows an exploded computer-aided-design view of the robot detailing the various components.

Chassis. ART's modular PVC chassis is composed of seven components: central tube, front and back T-sections (the front one is labelled as front viewport, where are camera may be installed), and four caps mounted on the ends of the T-sections (labelled shoulder joint to chassis mount). These caps have holes drilled in them to mount shoulder modules and allow cabling to pass through to the central tube where controllers are housed. Each of the PVC modules are press-fit together. Hot wax was applied around their mating interfaces for further waterproofing.

The robot is tethered to an external pressure supply (Porter Cable, Pancake Compressor A15414), power supply and computer for collecting data. The tether consists of silicone tubing (McMaster Carr, 3184K8) for the pneumatic lines, a 12-V, 10-A power supply cable a.c. adaptor for motor power (ROBOTIS), an extended universal serial bus cable for the data line and 22-gauge insulated copper wire (Amazon, TYUMEN Extension Wire) for the heaters. The tether emanates through a hole in the T-section at the tail end of the robot. We potted the hole around the cables with marine-grade epoxy (Amazon, Loctite 1919324 Marine Epoxy).

Shell. The robot's shell was fabricated in eight parts—four parts each for the top and bottom halves. Each shell part was 3D-printed with 100% infill polylactic acid (PLA) (Prusa i3 MK3). On the top and the bottom of the interior of the shell, we designed an offset groove to fit snugly around the curvature of the central tube of the PVC chassis. Two shell mounting holes, symmetrically on either side of the shell are included so that a pin can fix the shell into position. Slots for ballast are included on the bottom part of the shell.

Shoulder joint. A shoulder joint consists of three motors connected by aluminium brackets (ROBOTIS) in a configuration that allows the end effector to sweep through turtle-inspired aquatic and terrestrial gaits (Extended Data Fig. 1b). Having three motors in the shoulder allows controlled movements of forwards and backwards, up and down, and angle of attack, defined in Fig. 1c and Extended Data Fig. 1b as θ, ϕ and α, respectively. The motors that control these angles are, in order, Dynamixel MX-64, Dynamixel MX-106 and Dynamixel MX-64. The stall torque for the MX-64 series is 6 Nm, and for the MX-106 series, 8.4 Nm at constant operating 12 V. Each shoulder joint is surrounded by a 2-mm-thick stretchable rubber bellows that provides waterproofing for the motors and chassis while still allowing three degrees-of-freedom (DoF) movements. A port installed on the top of the chassis allows us to evacuate air from the bellows, decreasing their volume and effectively further tuning the robot's buoyancy. A 3D-printed offset shaft at the output of the angle-of-attack motor has the bellows sandwiched between its top (shoulder–limb interface) and bottom pieces. The other end of the bellows is wrapped around the diameter of one of the T-sections and clamped down with a ring clamp. The shoulder–limb interface terminating from the bellows provides a spot to mount limb modules.

Morphing limb. One limb module consists of a morphing limb attached to a 3D-printed interface, the limb–shoulder connector, that mates with the shoulder–limb interface. A limb is made in the fashion of ref. [22] (Extended Data Fig. 3). To summarize, elastomeric actuators of two different types, A and B, are cast in Dragon Skin 10 Slow (SmoothOn). Type A is longer and consists of two patterned chambers inducing axial curling and distal tip bending. Type B is shorter and only has internal chambers for axial curling. The two actuators are bonded to a strain-limiting layer of cross-ply fabric, given pneumatic tubing inlets, and a unidirectional lamina is then adhered to their surfaces to further direct deformation[34]. Next, thin and flexible foil copper-clad Kapton sheets (DigiKey) with the same contours as the actuators types A and B are ablated in a laser cut to form two serpentine heaters (LPKF lasers and electronics). These copper heaters are cast in a 10:4 by mass mixture of EPON 828 resin (Momentive Performance Materials) and Jeffamine D400 amine (Hunstaman International), degassed and cured at 60 °C for 12 h. The thermally activated variable-stiffness composites are then bonded to their respective actuators atop the fabric strain-limiting layer. Lastly, part A and part B sub-assemblies are sewn together along their edges. An aluminium rod is sewn to their newly shared leading edge, and the protruding end of the variable-stiffness composite is slid into the 3D-printed interface where epoxy is poured and to secure them in place. The limb module is then ready to mount to the shaft on the shoulder module.

Benefits conferred by the use of soft, stimulus-responsive materials in the morphing limb are as follows. First, the synthesized variable-stiffness polymer enables radical changes (450 times) in stiffness. This attribute permits low effort, in a bending-energy sense, to switch between flipper and leg shapes when the limb exceeds its glass transition temperature (T_g), as well as resilience in the final configuration on cooling.

Second, move-and-hold operations effectively eliminate the need to continuously supply pressure or some other actuation input (that is, voltage with an electrostatic clutch) to maintain a limb configuration during operation, enhancing safety and long-term energetic efficiency, and circumventing potential failure modes. Moreover, passively holding a morphed shape removes any control effort that would otherwise be needed to maintain a setpoint with alternative mechanisms.

Third, the chemistry of the limb materials allow for complex shape change. Being soft and continuously deformable past its T_g, the limb is able to assume compound curvatures across its length, generating both the cylindrical shell whose geometric stiffness facilities load bearing, as well as the curved limb tip that aids in traction and balance. Shapes are generated with disordered polymer networks that constitute a continuous, cohesive medium, whereas with conventional robotic components, such a task might require many interleaved components.

Finally, the limb is disposed to emerging facile manufacturing techniques and is made from readily commercially available, inexpensive materials. Morphing speed is a primary bottleneck for the proposed limb. Although it is possible to rapidly heat the limb past its T_g and actuate it, cooling to the final shape depends on the environmental temperature and the nature of the heat transfer boundary conditions. However, we are not particularly concerned with minimizing morphing times in the present work. Morphing lasts at maximum on the order of minutes, which is more than sufficient for effective transition between environments.

Treating the limb as a column under compression gives a simple mathematical explanation for its greater load-bearing capacity in the leg mode. Consider both the cross-sectional area (a) change and change in shape from approximately circular (leg) to hollow rectangular (flipper). The area moments of inertia for these cross-sections are:

$$I_{\text{leg}} = \frac{\pi}{4}(r_2^4 - r_1^4) \tag{1}$$

$$I_{\text{flipper}} = \frac{b_2 h_2^3 - b_1 h_1^3}{12} \tag{2}$$

For the leg cross-section, $a = \pi(r_2{}^2 - r_1{}^2)$; for the flipper, $a = b_2 h_2 - b_1 h_1$. Here, r_i are the inner or outer radii of the circular cross-section, and b_i and h_i are inner or outer widths and lengths of the rectangular cross-section. In our formulation, $i = 1$ refers to the smaller dimension. We consider the Euler critical buckling load of the limb, given by:

$$P_{\text{cr}} = \frac{\pi^2 EI}{(kL)^2} \tag{3}$$

where E is elastic modulus of the variable-stiffness material (this dominates the compression response compared with the silicone elastomer), I is the cross-sectional area moment of inertia, k is a length factor (assumed as 1 in a case for virtual pin boundaries on either side) and L is the unsupported length of the limb. Although k and E remain the same between leg and flipper mode, I changes from I_{leg} to I_{flipper}. The morphing operation is isoperimetric and constant thickness with respect to the limb's cross-section. Thus, the ratio between the two area moments of inertia, expressed in terms of the same set of parameters b_2, h_2 and t, assuming equivalent perimeters and thicknesses ($h_1 = h_2 - 2t$; $r_1 = r_2 - t$), gives:

$$I_{\text{leg}}/I_{\text{flipper}} = \frac{\frac{\pi}{4}\left(\left(\frac{2(b_2+h_2)}{2\pi}\right)^4 - \left(\frac{2(b_2+h_2)}{2\pi} - t\right)^4\right)}{\frac{b_2 h_2^3 - (b_2 - 2t)(h_2 - 2t)^3}{12}} \tag{4}$$

This ratio is always greater than 1 for fixed b_2, h_2 and t. A higher P_{cr} for the leg mode of the morphing limb makes it well suited to terrestrial locomotion, where gravitational loads must be supported. It is also noted how L slightly decreases in leg mode owing to the curling of the foot pad. This decrease in L further increases P_{cr}.

Operational power requirements. ART's power requirements vary depending on its environmental context, if it is moving and, if so, with what gait, as well as if it is undergoing morphing. Whereas morphing requires 50-W peak, maintaining upright posture requires a substantially lower 3-W peak. The computer used to control ART (64-bit Windows 10 on a Dell XPS 13 9343 with 2.4 GHz Intel core i7) was monitored using the Intel Power Gadget application. We noted a power draw of 5–7 W during operation. Compressed air at 30 kPa is sufficient for inflating the actuators while morphing; although compressor systems vary in their efficiency, the one we used mandates a peak 735 W at start-up. However, in practice, air is compressed beforehand, brought to the test site and attached to the robot. Thus we do not count this compressor power in the total live operational cost. During morphing, the robot does not move its motors, so power draw from motors is on the order of 1–3 W. We can assert that the maximum power requirement for running ART is the sum of heating (50 W), computer (7 W) and idle motors (3 W) contributions, in addition to a 5-W safety factor, which yields 65 W in total.

Kinematics, control and gait programming

The robot's forward kinematics were derived to (1) define a workspace, (2) visualize candidate gaits in a MATLAB simulation before implementing them on the physical robot, and (3) mirror the trajectory of one shoulder to the opposite side to render symmetric gaits. A Monte Carlo MATLAB simulation sweeping through joint angles bounded by the robot's hardware limits was conducted to visualize the workspace (Extended Data Fig. 2). The robot's modified Denavit–Hartenberg parameters are tabulated in Extended Data Table 1.

The robot runs on several Robot Operating System (ROS) nodes coded in Python that control motor-specific functionality. Each of robots' motors operates on an independent closed-loop position controller. Specifically, a proportional position controller with a gain of 32 was used.

To program swimming and crawling gaits, we rely on kinesthetic teaching: manually moving the robots' limbs while recording a rosbag to acquire the motors' trajectories. We sampled trajectories at a rate of 60 Hz and then post-processed the data by applying a moving average filter with a 20 sample window over the trajectory. The discrete set of motor position data, after it is processed, can be played back as a series of waypoints. The effect of the filter is to smooth the hand-programmed gaits. We used kinematic mirroring to take the hand-taught trajectory of one shoulder and transfer it symmetrically to the other shoulders, if applicable.

It is noted that, in contrast to actual turtles, ART's crawling gait uses all four limbs to propel itself forwards. Also, while crawling, ART employed its leg mode rather than the flipper because the flipper was too compliant to partially lift its body off the substrate.

We did not use kinesthetic teaching to program the creep gait, owing in large part to the asymmetry of the gait and need for coordination of multiple joints to produce forward locomotion while remaining statically stable. Thus, we programmed the creeping gait as a superposition of linear waypoints between encoder values, and then applied a running average filter over the waypoints to elicit smoother movements.

Calculation of COT

To calculate ART's average COT for both aquatic and terrestrial gaits, we used the relation considering the average electrical input power $\overline{P_{\text{in}}}$ to the robot:

$$\text{COT} = \frac{\overline{P_{\text{in}}(t)}}{mg\,\overline{v_{\text{bot}}}} \tag{5}$$

For our robot, the mass $m = 9$ kg and gravity $g = 9.81$ m s^{-1}. The robot's average velocity over five trials, $\overline{v_{\text{bot}}}$, was calculated from high-definition video at 30 fps and with a spatial resolution of 1 px mm^{-1}. The camera for recording video was positioned perpendicular to the robot's forward movement direction, approximately 4 m away, to capture the entire field of the robot's movement. The three types of motor on each of the shoulder joints contribute to the power input, via:

$$\overline{P_{\text{in}}(t)} = \sum_{i=1}^{4}\sum_{n=1}^{3}\overline{I_{n,i}(t)}V \tag{6}$$

where $I_{n,i}$ is the average amperage measured from the nth motor on the ith shoulder (in amperes) during the gait, and V is voltage supplied to the robot at a constant 12 V. Five trials of each gait were performed.

COT discussion. As evidenced by equation (5), the COT is a non-dimensional metric that is calculated by dividing average power input to a system by the product of mass, the local gravitational acceleration and average velocity. It describes the energetic cost to move a unit mass a unit distance. Alternatively, the total energy expenditure (E_{total}) can be divided by the product of the mass, the local gravitational constant and the total distance travelled (d):

$$\mathrm{COT} = \frac{E_{\mathrm{total}}}{mgd} \tag{7}$$

It is important to note that sometimes the COT is reported without dividing by g, resulting in a COT with units of J kg^{-1} m^{-1}, which further simplifies to s^2 m^{-1}. In other works on animals, the energy expenditure is expressed as V_{O2}, which is the volume of oxygen consumed during respiratory metabolism and the COT is reported as a having units similar to V_{O2} kg^{-1} × km, although V_{O2} can be converted to joules by taking its equivalent caloric value. In this paper, all COT values reported from previous work were converted into the unitless form defined as per equation (7). In addition, previous works take different approaches when measuring $P(t)$ or E_{total}, based on what is most practical to measure, and owing to this disparity some reported COT values cannot be compared.

When comparing COT values, it is important to consider which power or energy value is measured and what assumptions influence that measurement. Since at least the 1970s, metabolic COT and COT values derived from the energy input into the system, in our case the electrical COT, have been the standard metrics used for comparing biological and artificial systems.

When calculating COT for living organisms, respiratory metabolism is commonly used as a proxy for energy expenditure where the caloric value of V_{O2} is assumed to be the same as the system energy input. Several techniques are used for measuring oxygen uptake. In some experiments, animals have intravenous probes inserted into their arteries and sometimes veins.

In others, the entire volume of fluid entering and exiting an experimental chamber is tested in separate chambers to determine the gas composition. In more recent experiments, masks are fitted to the animals and the composition of the gas flows in and out are analysed.

In contrast, robotic systems often report two different types of COT. Some calculate COT using the total energy or power input to the system to propel the robot along a trajectory, such as the electrical power input ($P = IV$) or the potential chemical energy of the fuel consumed (J). Some robotic systems only measure the mechanical power at the end of the powertrain (often calculated via $P = \tau\omega$, where τ is the torque and ω is the angular velocity). The two types of COT differ by the inefficiencies between the input and output of the robot powertrains, and potentially other inefficiencies. For example, in a wheeled robot, the electrical power supplied to the motors from an external power source is larger than the mechanical power exerted by the wheels, differing by the efficiency of the powertrain. A COT calculated using electric power expended during movement will necessarily be higher than a COT calculated using the mechanical power exerted by the wheels. The same holds true for other energy inputs, such as chemical or pneumatic power supplies and their respective downstream actuators.

ART's average forward velocity and COT for different substrates and gaits are tabulated in Extended Data Table 2. For a biological comparison, sea turtles exhibit typical cruising speeds of 0.5–0.6 m s^{-1} (ref. [35]). Galapagos tortoises have been found to walk at 0.16 m s^{-1} (ref. [21]), although this value has a large range depending on conditions. The COT of hatchling and juvenile sea turtles (*Chelonia mydas*) ranges between 0.3 and 2 (refs. [20,36]) when swimming, whereas that of the semi-aquatic Macquarie turtle (*Emydura macquarii*) ranges between 0.2 and 0.6 (ref. [37]) when walking. The discrepancy in speeds and COT between actual turtles and ART is partly attributable to the lower energy density, efficiency, elastic energy storage and power output of transmission-based servomotors compared with animal muscle[38]. Gaits were programmed by observing animals' gaits and are consequently not optimized. Further tuning gait parameters to minimize extraneous movements might improve speed and COT.

Swimming tests

Swimming tests were conducted in a large outdoor pool ($l \times w \times d$ = 15 m × 8 m × 5 m). Operational Reynold's numbers for the robot, defined as

$$\mathrm{Re} = \frac{Ul}{\gamma} \tag{8}$$

where U is the velocity of the fluid, l is the length of the robot and γ is the kinematic viscosity, ranging between 6.4×10^3 and 2.6×10^4 for all aquatic gaits tested. This Re falls within a similar range as leatherback hatchlings with l = 0.08 m at Re = 7.2×10^3 for slow sustained swimming and Re = 2.7×10^4 for vigorous swimming[39]. Compare this with grown leatherback sea turtles with l = 1 m, operating at Re = 5×10^5 (ref. [40]).

Free swimming tests for calculating the COT were conducted along the length of a pool, while recording the velocity of the robot with a high-definition camera. Two gaits, paddling and flapping, were studied. We varied the offset angle (Fig. 2b) of the flapping gaits from 10° to 40° in increments of 5°. Before 10°, the robot exhibited no forwards displacement.

The regions of Fig. 2b were determined as follows, after collecting COT data from flapping across a span of angles. The first (red) region was determined by partitioning where COT of flapping was higher than that of paddling. The second (yellow) region was at first empirically demarcated because it exhibited a steep drop in COT; subsequent computational fluid dynamics simulations ('Computational fluid dynamics simulation of flipper') demonstrated that this region corresponds to a critical shift in angle of attack that reduces drag throughout the stroke. The third (blue) region was delineated because it witnesses a decrease in slope of the trend line as the COT approaches its best value.

To assess the force profile of paddling and flapping gaits, a custom-designed test rig (Extended Data Fig. 4b) was constructed on which to mount the robot and measure forces using a multi-axis transducer (ATI Industrial Gamma F/T sensor). The test rig was affixed to the side of a pool and the robot was attached 0.635 m submerged and 2 m offset from the pool walls and bottom to mitigate boundary effects. The robot being fixed prevents analysis of the dynamics of a full propulsion cycle, and therefore we cannot make any conclusions about the steady state or transient quality of flow about the robot. We can, however, still gain insight into the magnitude and direction of forces exerted during each type of gait. While a gait was executed, we sampled x- and z-direction forces (Extended Data Fig. 4) at a rate of 1,000 Hz using a data acquisition unit (National Instruments USB-6212). Five trials of each gait were performed. Extended Data Fig. 5 shows one set of representative commanded and actual angular displacements, speeds and motor amperages corresponding to the force profiles of the paddling and flapping gaits shown in Fig. 2c,d.

Computational fluid dynamics simulation of flipper

We conducted a numerical analysis in ANSYS Fluent to examine the lift (normal to flow direction) and drag (parallel to flow direction) forces on the limb during the downstrokes and upstrokes of the flapping gait, at a condition with a flow rate of 0.3 m s^{-1}. A speed of 0.3 m s^{-1} is approximately the robot's peak speed at the upstroke; at this moment, the flipper's angle of attack will have the strongest influence over drag forces than any other time in the stroke, owing to the increased relative velocity between robot and fluid.

Steady-state simulations, parametrically varying the angle of attack as $0° \leq \Phi \leq 60°$ in increments of 5°, were conducted with an .IGS model of the flipper, placed in the centre of a virtual flow domain. The flow domain was modelled as a 2-m-long cylindrical volume with inlet and outlets of area 3.141 m^2. Meshing for the flipper and flow domain employed adaptively sized tetrahedral elements, rendering a computational domain of approximately 1,000,000 cells. The boundary condition was set to mass flow rate in equal to mass flow rate out of the entrance and exit to the cylindrical volume. For the calculation, we selected the Fluent computational fluid dynamics (CFD) solver with the method as SIMPLEC. A solution was initialized at $v = 0$ m s^{-1} in the direction of flow. To determine convergence, we monitored forces of lift and drag, as well as the flow-direction velocity, with convergence occurring if these metrics dipped below 0.001 residual value.

CFD results. Before we discuss the CFD results, we first define Φ as the angle of attack of the flipper relative to the flow direction (Extended Data Fig. 6, inset). Recall that α measures the angular displacement of the terminal motor in the shoulder joint, in the kinematic chain's frame of reference (Extended Data Fig. 1). Therefore, Φ and α do not necessarily coincide. Lastly, as defined in the main text, $\bar{\theta}$ is a scalar offset applied to α for the duration of the stroke.

The results of the simulation reveal a typical hydrofoil response for the flipper (Extended Data Fig. 6). A peak in lift force occurs around $\Phi = 15°$, quickly followed by a region of stall. Drag forces are monotonically increasing with Φ in a nearly linear fashion. In the yellow region of Fig. 2b, the steeper drop in COT corresponds to a favourable angle-of-attack offset, $\bar{\theta}$.

By analysing the flapping gait's kinematics and the results of simulation, we can predict what factors cause this drop in the COT. During the flapping gait's upstroke, the flipper is used essentially as a paddle to push back the water. Increasing θ makes Φ higher with respect to the flow direction (the robot is pushing back, so net flow about the flipper occurs in the defined positive direction of Extended Data Fig. 4), thereby allowing the robot to produce more effective thrust on the upstroke. At the end of the upstroke and before the beginning of the downstroke, the flipper slows down while the robot glides forwards. During this part of the gait cycle, increases to θ move the flipper to closer to $\Phi = 0°$ with respect to the flow direction (which is now opposite to the defined forward direction of Extended Data Fig. 4), reducing drag. Furthermore, angles between $0° < \Phi < 15°$ cause the generation of some lift force; its vector component in the forwards direction can help maintain speed through to the next portion of the gait, the downstroke. During the downstroke, the robot moves its flipper slightly rearwards. In this scenario, it is again favourable to have a higher Φ against the forwards direction to produce more thrust, whereas angles between $0° < \Phi < 15°$ may generate a vector component of lift in the forwards direction.

In summary, a favourable $\bar{\theta}$ puts the flipper at higher Φ during quasi-paddling sections of the gait cycle, and orients it between 0° and the peak angle before stall in gliding after an upstroke or downstroke. This is why we see the COT decreasing with increasing θ. However, this will not be a monotonically decreasing trend for even higher values of θ. Eventually θ will exceed a value where it is generating net counterproductive thrust, as it did before 10°. In our case, hardware constraints of the bellows twisting too much capped the tenable angle-of-attack offset at $\bar{\theta} = 40°$, and thus we did not test past this value.

Terrestrial tests

Terrestrial tests took place on flat porcelain tile inside the lab, and concrete or granite in an outside environment. COT and P_{in} were calculated in the same fashion as with aquatic gaits, as per equations (5) and (6). We used Ascension trakSTAR (Ascension Technology Corporation (an NDI company)) motion tracking markers to monitor the 6-DoF of ART's limb trajectory on the different substrates.

For calculating the stability metric, $\mathcal{S}$, we used the disparity between the actual z-axis trajectory and an ideal trajectory of the robot with enforced perfect ground contact. The ideal trajectory as the robot pivots or resides in a stance phase is a constant line of zero slope. In other words, an ideal trajectory entails no slip, intermittent ground contacts, or splay/tucking in of the legs, all of which may decrease force generated for forwards locomotion. Projected z-axis data used in the calculation of $\mathcal{S}$ started after the robot completed a 'step BL' phase (Fig. 3b,d). Data were normalized to start at a value of 0. An average value for $\mathcal{S}$ was calculated over five trials.

Terrestrial locomotion analysis. The robot's stride frequency and length while creeping depended on the substrate it was traversing. For the porcelain control substrate, the stride frequency was 0.145 strides per second averaged over the entire data collection period. Three-dimensional motion capture data collected of creeping on different substrates revealed consistency in terms of stride length and swept trajectory. In the cases of porcelain, concrete and granite, the stride length was 0.182 m ± 0.015 m, 0.217 m ± 0.022 m and 0.206 m ± 0.027 m, respectively.

Extended Data Fig. 7 shows the commanded and actual positions for the creep gait over porcelain, for each of the four shoulder joints. Extended Data Fig. 8a gives plots for the front-right shoulder joint over porcelain. Extended Data Fig. 9 shows the same for the crawl gait, but only focuses on one shoulder joint owing to symmetry.

Of particular relevance to limbed locomotion offset from the ground—in our case, the creep gait—is the Froude number, a quantity that helps classify animals across different sizes into groups that locomote similarly. It is the ratio of the centripetal force around the centre of motion—the foot—and the weight of the entity walking:

$$F_R = \frac{U^2}{gh} \tag{9}$$

where U is the forwards velocity of the robot, g is the acceleration owing to gravity and h is the height of the robot's hip joint from the ground (0.3 m). The average Froude number for the creeping gait across substrates was 2.9×10^{-4}. It is interesting to note that this number is lower than the range characteristic of terrestrial vertebrates and tortoises[21]. ART's legs are longer than actual turtles' legs, and this caused some stability issues when trying to creep on the granular substrates. Moreover, unlike most quadrupedal robots, ART uses 2-DoF for each leg when walking. Although somewhat restrictive in terms of upright movement, this design choice was intentional for preserving the critically important angle-of-attack DoF in the swimming kinematic configuration, and simultaneously minimizing the hardware required for locomotion across multiple environments.

Transition-substrate tests

For transition-substrate tests, we filled a sandbox with the substrate to a depth of 101.6 mm, for 0.34 m^3 volume of substrate. The sand used was Pavestone patio/paver sand with a granule diameter distributed between 0.08 mm and 2.4 mm, average 0.4 mm. All dry substrates were at 22 °C. We also made an intertidal substrate consisting of pebbles (Vigoro decorative stone: all-purpose stone; diameter distributed between 20 mm and 100 mm, average 50 mm), sand and water mixed together. First, 15% water by volume was mixed with the sand. Then we added 15% by volume pebbles to the sand/water mixture.

A complex interaction between several factors including flipper thrust generated by pushing through the fluid-like medium, body lift, base drag, ground yielding and texture of the ground governs turtles' locomotion over granular media[17]. We considered that friction was a main contributor to the robot's performance over the different substrates when crawling. To test this hypothesis, we conducted friction tests between the three substrates and PLA, elastomer and the rubber

bellows to quantify the coefficient of static friction between each. A rectangular specimen of the material with a fixed surface area was attached to a low-friction string, routed through a pulley, and mounted to the load-head of a materials testing machine (Instron). Atop this material specimen, we applied distributed weight. Applying 150 mm min^{-1}, the specimen with weight atop was dragged along either porcelain (control), sand or the intertidal substrate. Force and displacement data were recorded. For a given material–substrate pairing, we conducted seven independent tests. The static coefficient of friction was calculated as:

$$\mu = F_m/W \quad (10)$$

where F_m is the force at the initial specimen movement and W is the weight of the rectangular material specimen plus the additional distributed mass atop. As the robot varies its weight exertion on the substrate depending on the exact moment in the stroke cycle, we tested a range of weights from 50 g to 1 kg. We noticed a dependence of the coefficient of friction on the weight used. The average of μ for all weights was reported for a given substrate–material pairing. Extended Data Fig. 10 gives representative test data averaged over seven cycles for the 500-g mass used in the calculation of μ.

A positive correlation between μ (between primary contact interfaces, PLA or elastomer, and substrates) and the COT for crawling validates that μ is a reasonable predictor of performance for the crawling mode of locomotion. Although it is likely that the bellows made some contribution to the forces during locomotion, we expect that the robot's primary contact interfaces have a much more dominant contribution. Consider that the majority of the bellows' surface area that is touching substrate does so lightly, and this surface area consists predominately of creases and folds, not a flush interface. A smaller normal force arises from the bellows, which will yield a lower friction force. In contrast, the PLA shell and elastomer limb bear more of the robot's weight, have greater surface areas that are more directly in a shear with the substrate and are more rigid, so we expect these primary interfaces to be the source of most of the forces. The μ values for all substrate–interface combinations is tabulated in Extended Data Table 3.

Transition-substrate gait considerations. In preliminary experiments, we found that a four-limb crawl was more effective in generating forwards thrust and speed than using two limbs. Thus, for the present paper, ART implements a four-limbed crawl for transition-substrate locomotion. Actual sea turtles do not have the functional shapes or musculature to perform such a gait, and predominately generate thrust with their fore flippers when beaching. ART's marked departure from its biological inspiration in this respect underscores its advantages as a synthetic system capable of 'unnatural' yet highly effective locomotion modes. As creep is characterized by totally different mechanics, we note the importance of substrate yield stress and penetration depth, and how these factors are influenced by fluidization and disperse grain sizes.

Morphing tests

The variable-stiffness composite is waterproof to facilitate morphing in wet environments. We sought to quantify how the different free convection conditions of being submerged in water or in air would influence the softening of the variable-stiffness material through Joule heating. We conducted morphing tests in water and in air, both at 22 °C (Supplementary Videos 3 and 4). The water test was conducted in a large bin filled with tap water that was allowed to reach room temperature of 22 °C. With the limb morphed into the leg mode, the test entailed subjecting each heater to 50 W, supplied from an external power supply, while recording high-definition video to monitor deformation of the limb. The limb took around 100 s to morph in water and 50 s to morph in air.

Field tests

We took the robot to East Rock Park, in New Haven, CT, for field testing in a natural intertidal transition environment. The shoreline featured hard-packed dirt with various-sized pebbles and sticks. Closer to the water, fluidized sand and mud were pervasive. The water was partially saline, exhibited weak currents and had a peak depth of 1 m. The robot was powered from a Honda 2,500-W invertor generator. In previous tests, a tether consisting of data and power lines was employed. For field testing, we extended the pneumatic and heater lines into the tether.

Our first time testing ART occurred in autumn, with an air temperature of 5 °C and a water temperature of 9 °C. Locomotion and shape policies were chosen by an operator on-site based on data from land, transition-substrate and aquatic tests. We attempted to morph the limbs while they were submerged to no avail, probably owing to the high heat transfer owing to forced convection of the cold water. We decided it would be energetically expedient to conduct morphing out of the water during field tests and to wait until a warmer season. The second test occurred in spring, with an air temperature of 23 °C and a water temperature of 15 °C. This time, we were able to achieve morphing by programming ART's limbs to lift up.

Challenges that became apparent during the transition included difficulty transitioning from water to land—the robot needed to beach itself entirely, then perform a push-up, which the motors were not strong enough to do. Alternatively, the robot could try and orient its legs in the shallows, but currents and debris underfoot destabilized the robot such that it could not stay balanced. Transition from water to land thus remains an area for future work.

COT comparison chart

In Fig. 5b, the COTs for insects, reptiles, birds, mammals and other robots were either directly reported, or obtained and replotted from refs. [29,37,41–53] using graph digitizing software (GetData v2.25).

Data availability

All data needed to evaluate the conclusions in the paper are present in the paper and/or the Supplementary Information.

31. Mahadevan, L. *Morphogenesis: Geometry, Physics, and Biology* (Perimeter Institute for Theoretical Physics, 2021).
32. Ultee, E., Ramijan, K., Dame, R. T., Briegel, A. & Claessen, D. Stress-induced adaptive morphogenesis in bacteria. *Adv. Microb. Physiol.* **74**, 97–141 (2019).
33. Justice, S. S., Hunstad, D. A., Cegelski, L. & Hultgren, S. J. Morphological plasticity as a bacterial survival strategy. *Nat. Rev. Microbiol.* **6**, 162–168 (2008).
34. Kim, S. Y. et al. Reconfigurable soft body trajectories using unidirectionally stretchable composite laminae. *Nat. Commun.* **10**, 3464 (2019).
35. Kinoshita, C., Fukuoka, T., Narazaki, T., Niizuma, Y. & Sato, K. Analysis of why sea turtles swim slowly: a metabolic and mechanical approach. *J. Exp. Biol.* **224**, jeb236216 (2021).
36. Butler, P., Milsom, W. & Woakes, A. Respiratory, cardiovascular and metabolic adjustments during steady state swimming in the green turtle, *Chelonia mydas*. *J. Comp. Physiol. B* **154**, 167–174 (1984).
37. Baudinette, R. V., Miller, A. M. & Sarre, M. P. Aquatic and terrestrial locomotory energetics in a toad and a turtle: a search for generalisations among ectotherms. *Physiol. Biochem. Zool.* **73**, 672–682 (2000).
38. Madden, J. D. Mobile robots: motor challenges and materials solutions. *Science* **318**, 1094–1097 (2007).
39. Davenport, J. Locomotion in hatchling leatherback turtles *Dermochelys coriacea*. *J. Zool.* **212**, 85–101 (1987).
40. Eckert, S. A. Swimming speed and patterns of leatherback turtles. *J. Exp. Biol.* **205**, 3689–3697 (2002).
41. Tucker, V. A. Energetic cost of locomotion in animals. *Comp. Biochem. Physiol.* **34**, 841–846 (1970).
42. Long, J. H., Schumacher, J., Livingston, N. & Kemp, M. Four flippers or two? Tetrapodal swimming with an aquatic robot. *Bioinspir. Biomim.* **1**, 20–29 (2006).
43. Chen, Y., Doshi, N., Goldberg, B., Wang, H. & Wood, R. J. Controllable water surface to underwater transition through electrowetting in a hybrid terrestrial–aquatic microrobot. *Nat. Commun.* **9**, 2495 (2018).
44. Wang, G. et al. Subsea crab bounding gait of leg-paddle hybrid driven shoal crablike robot. *Mechatronics* **48**, 1–11 (2017).
45. Sellers, W. I., Rose, K. A., Crossley, D. A. & Codd, J. R. Inferring cost of transport from whole-body kinematics in three sympatric turtle species with different locomotor habits. *Comp. Biochem. Physiol. A* **247**, 110739 (2020).

46. Milana, E. et al. EELWORM: a bioinspired multimodal amphibious soft robot. In *2020 3rd IEEE International Conference on Soft Robotics (RoboSoft)* 766–771 (IEEE, 2020).
47. Kitano, S., Hirose, S., Horigome, A. & Endo, G. TITAN-XIII: sprawling-type quadruped robot with ability of fast and energy-efficient walking. *ROBOMECH J.* **3**, 8 (2016).
48. Kandhari, A., Wang, Y., Chiel, H. J., Quinn, R. D. & Daltorio, K. A. An analysis of peristaltic locomotion for maximizing velocity or minimizing cost of transport of earthworm-like robots. *Soft Robot.* **8**, 485–505 (2021).
49. Kau, N., Schultz, A., Ferrante, N. & Slade, P. Stanford Doggo: an open-source, quasi-direct-drive quadruped. In *2019 International Conference on Robotics and Automation (ICRA)* 6309–6315 (IEEE, 2019).
50. Berlinger, F., Saadat, M., Haj-Hariri, H., Lauder, G. V. & Nagpal, R. Fish-like three-dimensional swimming with an autonomous, multi-fin, and biomimetic robot. *Bioinspir. Biomim.* **16**, 026018 (2021).
51. Kim, K., Spieler, P., Lupu, E.-S., Ramezani, A. & Chung, S.-J. A bipedal walking robot that can fly, slackline, and skateboard. *Sci. Robot.* **6**, eabf8136 (2021).
52. Bledt, G. et al. MIT Cheetah 3: design and control of a robust, dynamic quadruped robot. In *2018 IEEE/RSJ International Conference on Intelligent Robots and Systems (IROS)* 2245–2252 (IEEE, 2018).
53. Hutter, M. et al. ANYmal—a highly mobile and dynamic quadrupedal robot. In *2016 IEEE/RSJ International Conference on Intelligent Robots and Systems (IROS)* 38–44 (IEEE, 2016).
54. Craig, J. J. *Introduction to Robotics: Mechanics & Control* (Addison-Wesley, 1986).

Acknowledgements We thank V. Wilczynski, Deputy Dean of Yale School of Engineering, for use of his pool. This project was sponsored by the Office of Naval Research under award N00014-21-1-2417. Any opinions, findings, and conclusions or recommendations expressed in this material are those of the authors and do not necessarily reflect the views of the Office of Naval Research. R.B. was supported by an NSF Graduate Research Fellowship (DGE-1752134).

Author contributions R.B., S.K.P., J.B., T.S. and A.G. designed and built the robot. R.B., S.K.P. and L.R. conducted swimming, terrestrial and transition experiments. R.B., S.K.P., L.R. and F.F. programmed gaits. R.B. conducted CFD simulations and friction tests. R.K.-B. conceived of the project and oversaw the research. All authors contributed to writing the manuscript.

Competing interests The authors declare no competing interests.

Additional information

Supplementary information The online version contains supplementary material available at https://doi.org/10.1038/s41586-022-05188-w.

Correspondence and requests for materials should be addressed to Rebecca Kramer-Bottiglio.

Peer review information *Nature* thanks Navinda Kottege and Cecilia Laschi for their contribution to the peer review of this work. Peer reviewer reports are available.

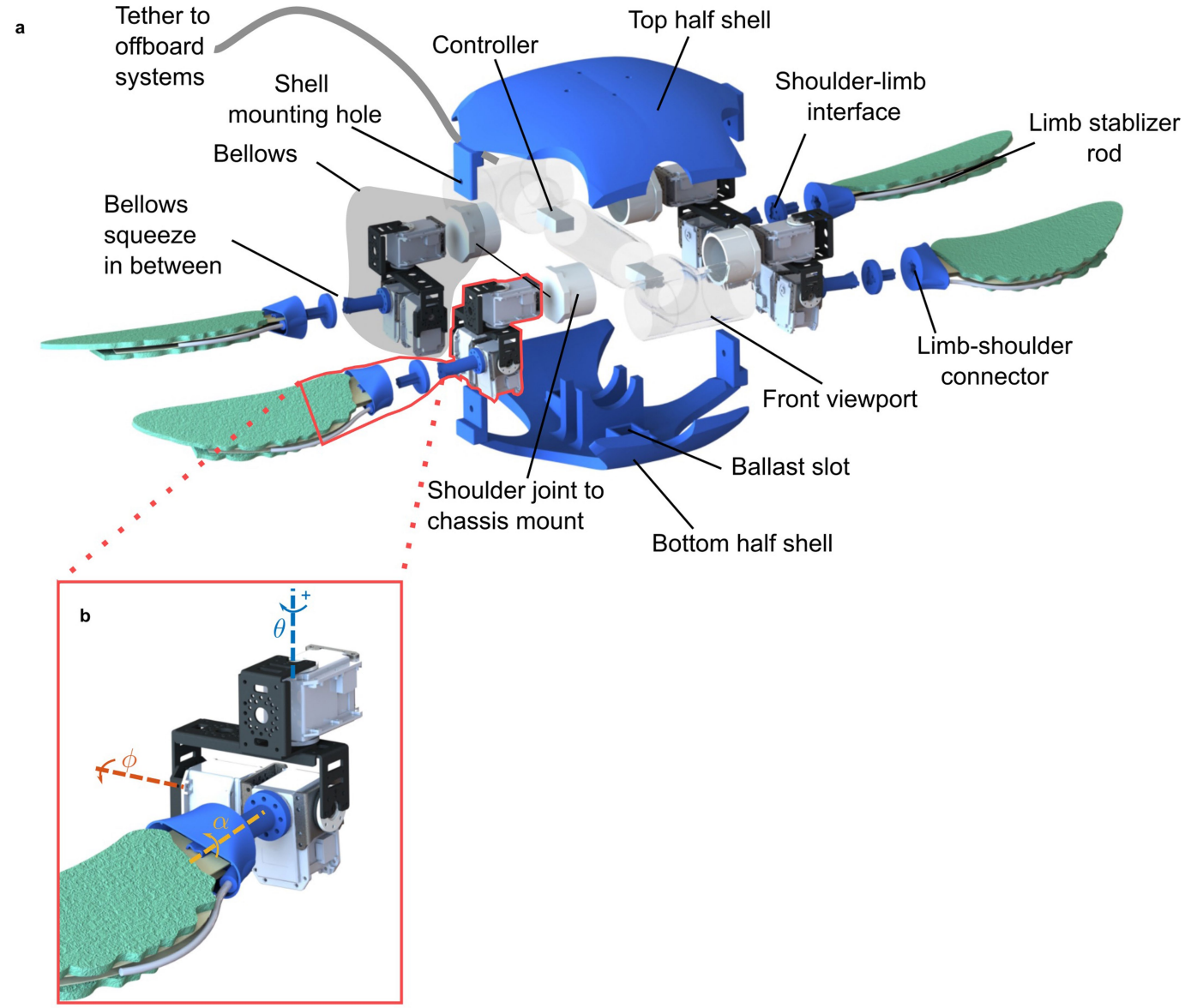

Extended Data Fig. 1 | System description. a, Exploded computer-aided-design view, detailing components of robot. Note that the shoulder joints are typically shrouded in rubber bellows, and thus not visible. For clarity, we only depict the bellows on the back right joint in transparent grey. **b**, 3-DoF kinematic mechanism used to achieve bio-inspired gaits. Symbols θ, ϕ and α are the rotation axes for the swing forward/backward, up/down, and angle of attack motors, respectively.

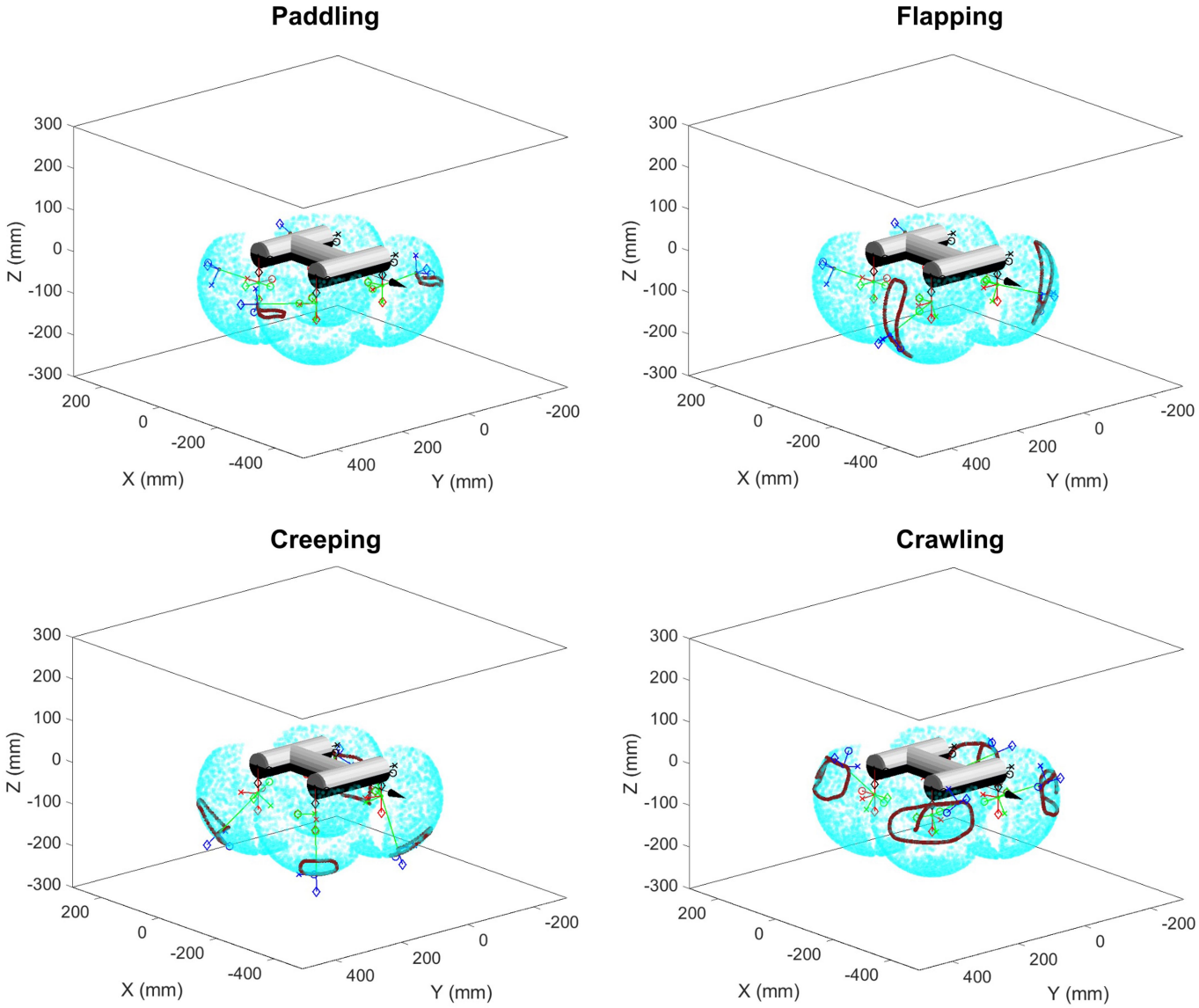

Extended Data Fig. 2 | Robot workspace. Workspace visualized in the robot's kinematic simulation. The explored gaits are superimposed atop the cyan workspace in a darker colour. Top two are swimming gaits; bottom two are terrestrial and transition gaits. Chassis beneath the shell is rendered for context. Links are line segments coloured red, green, and blue. The black arrow points in the forward travel direction.

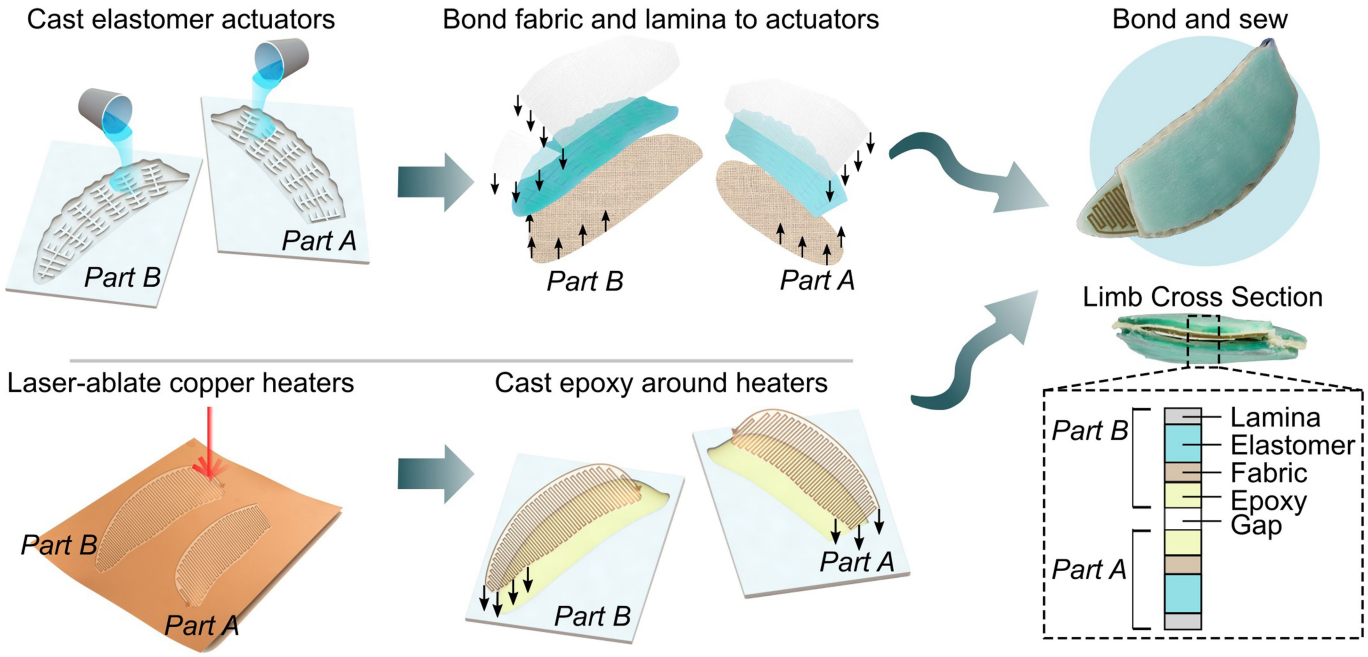

Extended Data Fig. 3 | Fabrication of Morphing Limb. Fabrication can be broken down into two main tracks: elastomeric actuators (top), and Joule-heating variable-stiffness material (bottom). We fabricate components for each of the limbs' two halves, A and B. Actuators and variable-stiffness material components for A and B come together in the final step, in which they are hinged together via a sewed joint. The limb cross-section is displayed in the inset. Figure and caption adapted from ref. [22].

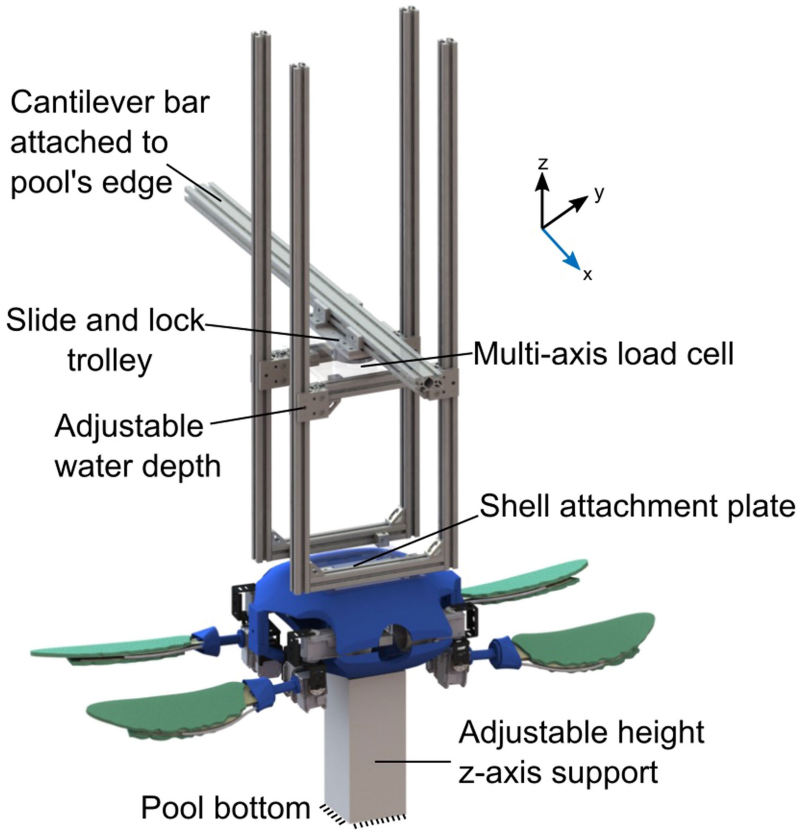

Extended Data Fig. 4 | Test rig for evaluating force profiles of gaits. Coordinate system defines positive direction of forces measured via the multi-axis load cell. Adjustable fixtures allowed us to tune the robot's offset from the pool sides and bottom, as well as its submerged depth.

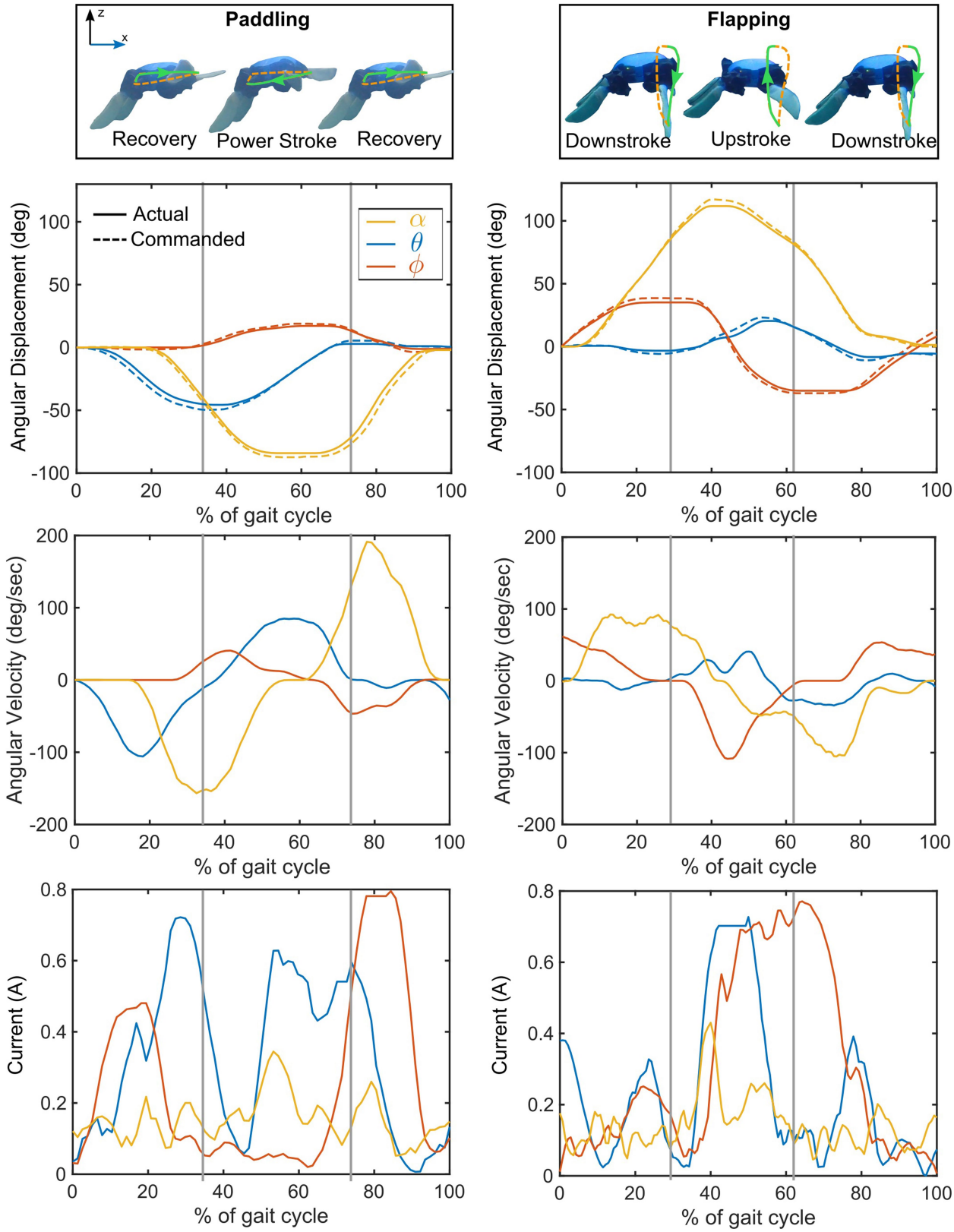

Extended Data Fig. 5 | Representative data for front-right shoulder during paddling and flapping gaits. Top row gives a robot schematic with superimposed trajectory. Second row gives commanded and actual encoder positions, where the solid line is the actual achieved position. Third row plots the angular velocity. Fourth row is the amperage. Line colour and legend symbols match those of Fig. 1b.

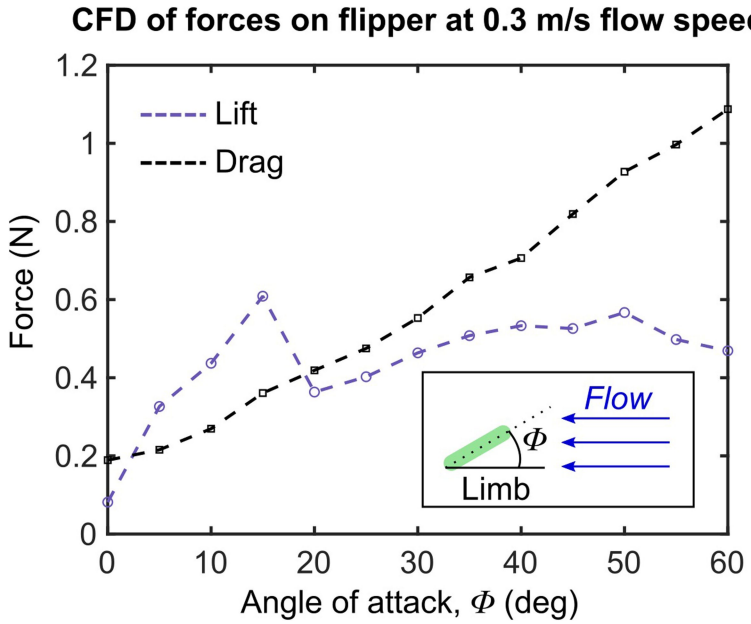

Extended Data Fig. 6 | CFD results. Simulation results of lift and drag forces on the flipper mode of the morphing limb, at 0.3 m/s. Inset depicts definition of Φ with respect to the flow direction.

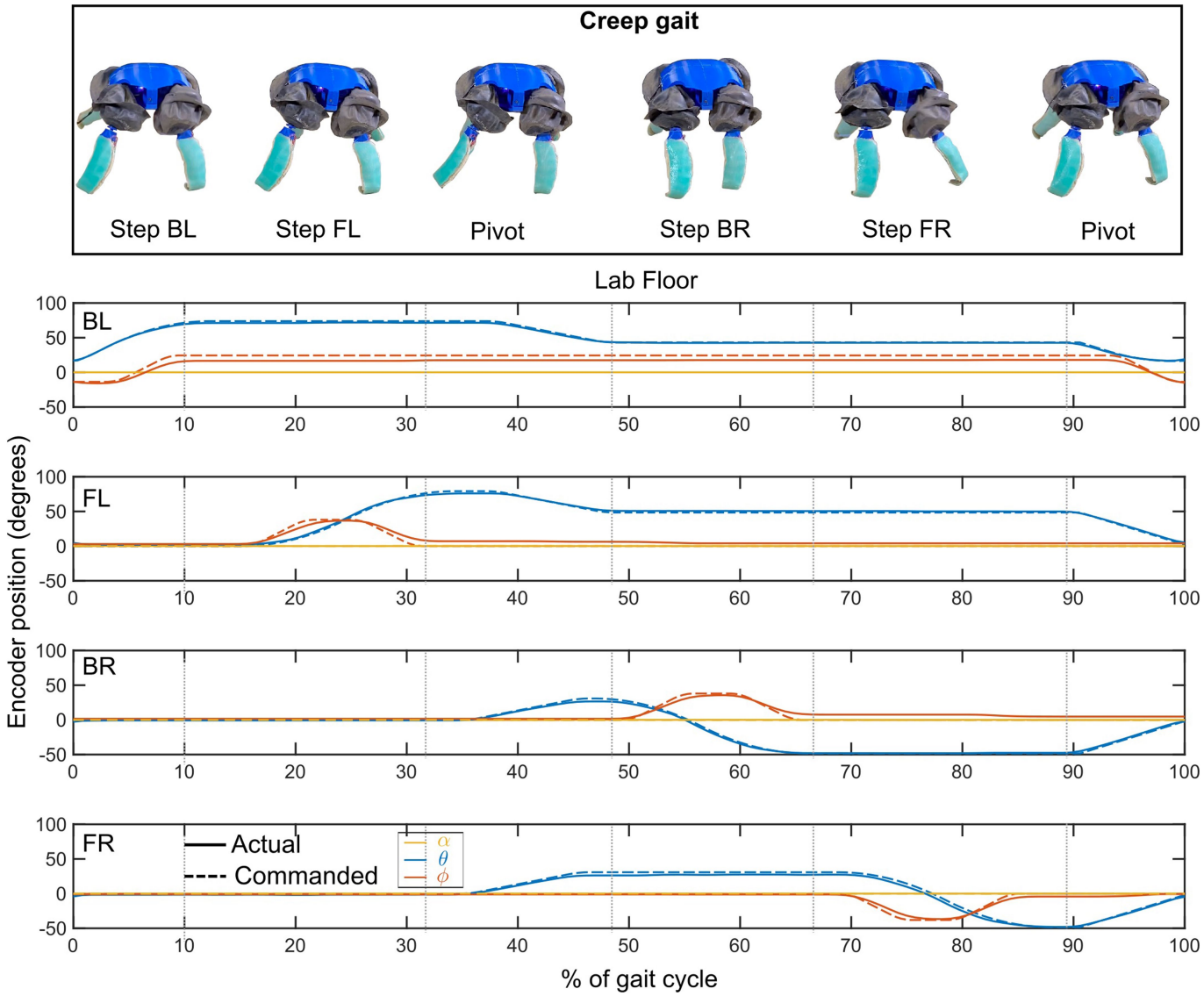

Extended Data Fig. 7 | Representative data from all shoulder joints for creeping gait on the porcelain substrate. Top row presents snapshots of the robot at key parts of the gait. Graphs underneath give commanded and actual encoder positions, where the solid line is the actual achieved position. Line colour and legend symbols match those of Fig. 1b.

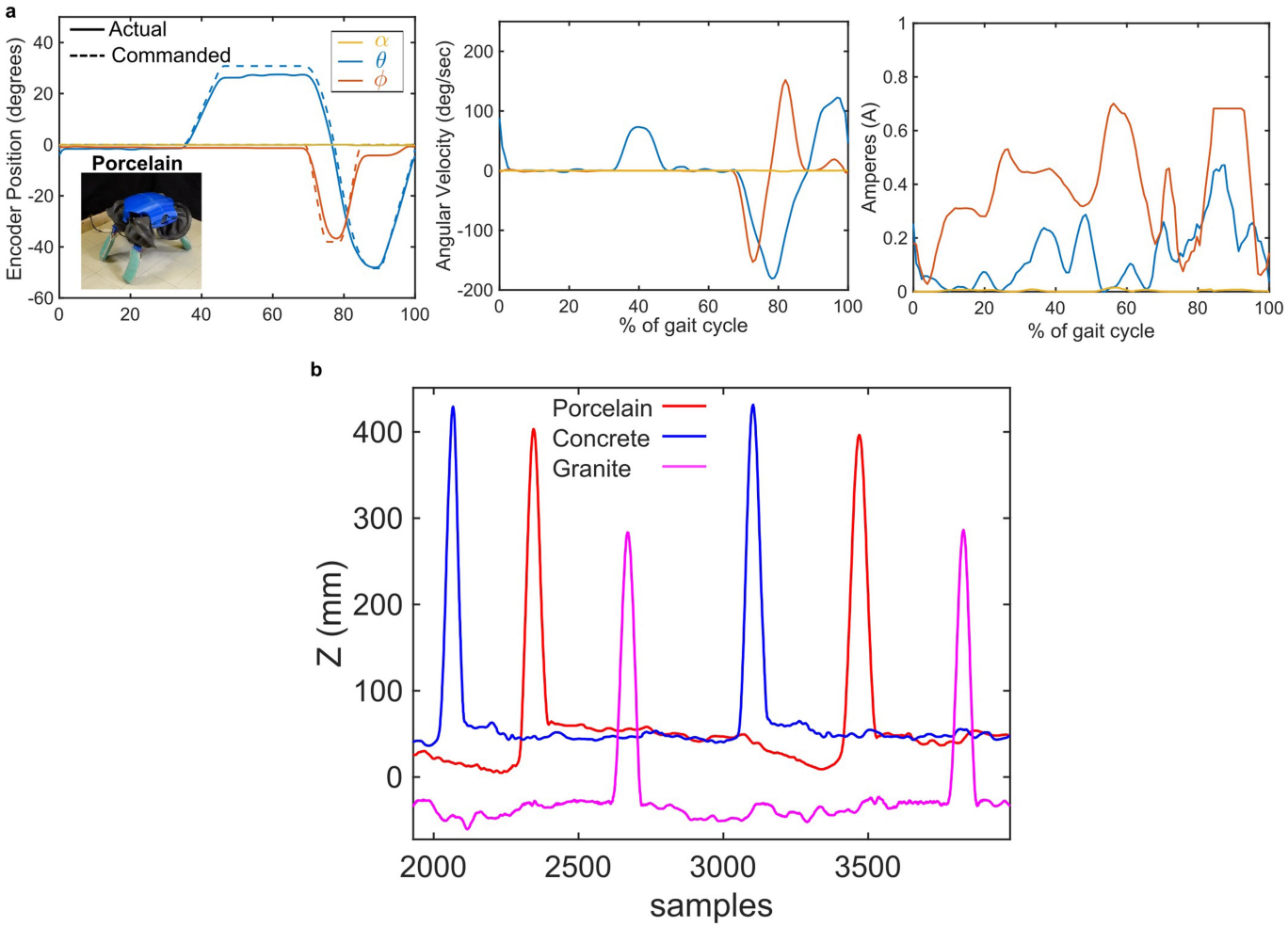

Extended Data Fig. 8 | Additional creep data. a, Left to right: commanded and actual encoder positions, angular velocity, and amperage for front-right shoulder joint. The solid line is the actual achieved position. Line colour and legend symbols match those of Fig. 1b. **b**, Representative data from motion capture of back-left distal tip of limb during creep gait. Spikes in Z correspond to the limb swinging out, whereas the other portions are the pivot or where the limb serves only to balance the robot. Notice the amplitude and frequency of vibrations occurring at these times, which give an indication of surface normals and roughness. At these sections, we calculated the stability metric to grasp the effect of substrates on COT when creeping. Here, the series are not normalized to all start at 0, for ease of viewing.

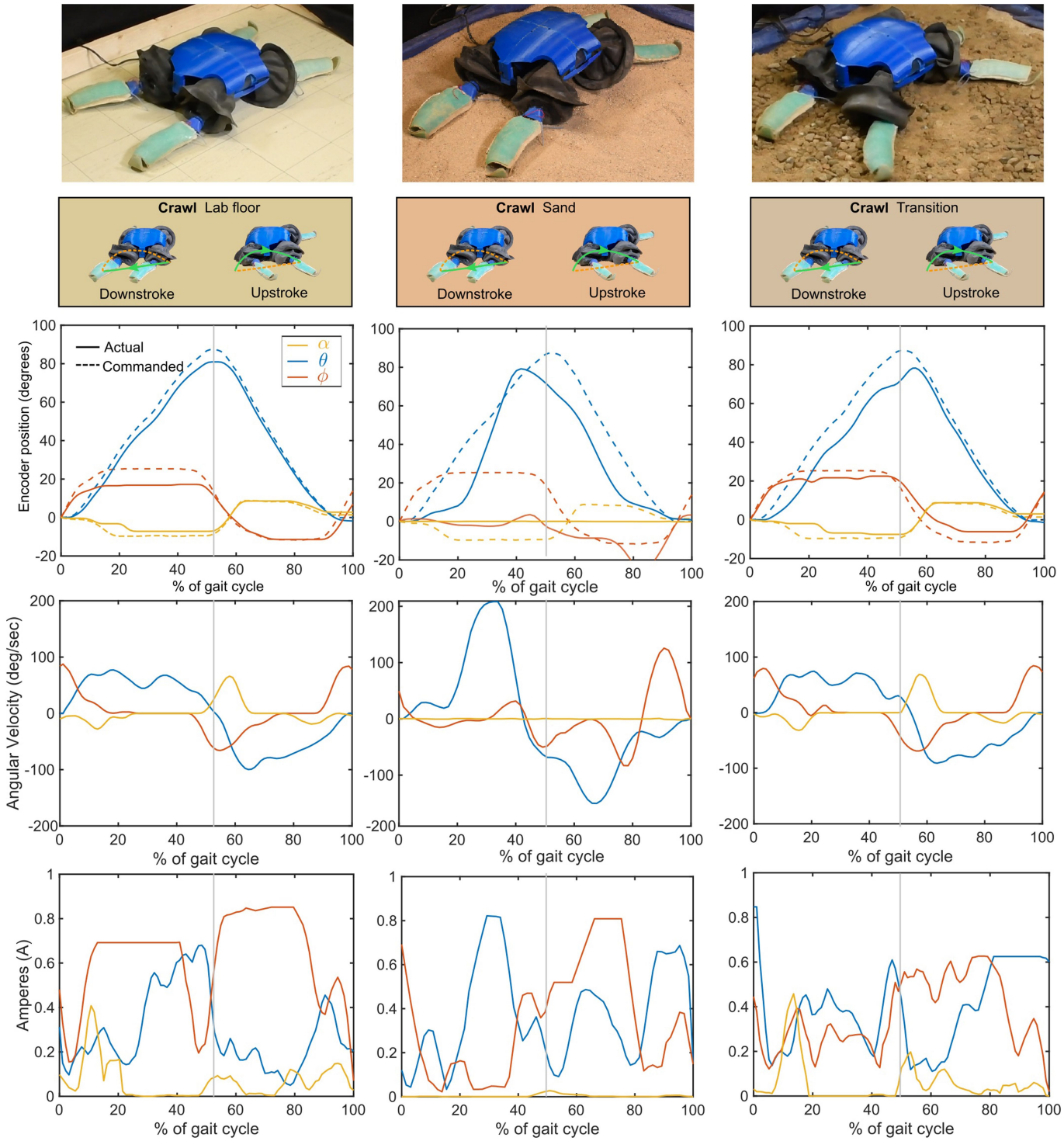

Extended Data Fig. 9 | Representative data from front-right shoulder joint for crawl gaits across the three substrates. Top row gives a robot schematic with superimposed trajectory. Second row gives commanded and actual encoder positions, where the solid line is the actual achieved position. Third row plots the angular velocity. Fourth row is the amperage. Line colour and legend symbols match those of Fig. 1b.

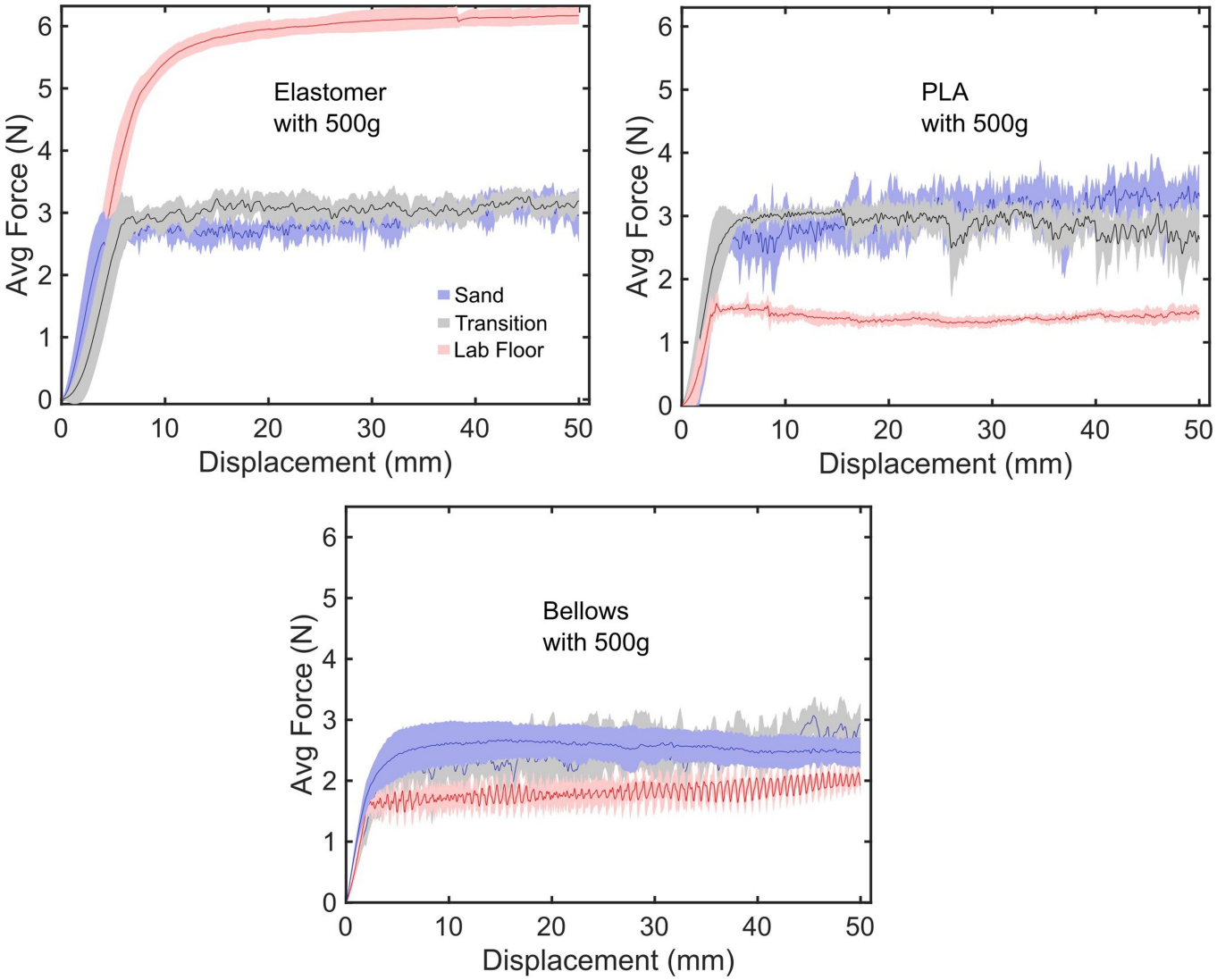

Extended Data Fig. 10 | Example data from friction tests. Force versus displacement for elastomer, PLA, or bellows with 500 g weight placed atop them, over the various substrates. Clouds indicate one standard deviation from the mean, over 7 trials, with the solid line as the mean.

Extended Data Table 1 | The robot's modified Denavit–Hartenberg parameters[54]

Link (FL)	α_{i-1}	a_{i-1}	d_i	θ_i
1	0	0	d_1	θ_1
2	$-\pi/2$	0	0	$-\theta_2+\pi/2$
3	$\pi/2$	0	d_3	θ_3

Link (FR)	α_{i-1}	a_{i-1}	d_i	θ_i
1	0	0	d_1	θ_1
2	$-\pi/2$	0	0	$-\theta_2+\pi/2$
3	$-\pi/2$	0	d_3	θ_3

Link (BL)	α_{i-1}	a_{i-1}	d_i	θ_i
1	0	0	d_1	θ_1
2	$\pi/2$	0	0	$-\theta_2-\pi/2$
3	$-\pi/2$	0	d_3	θ_3

Link (BR)	α_{i-1}	a_{i-1}	d_i	θ_i
1	0	0	d_1	θ_1
2	$\pi/2$	0	0	$-\theta_2-\pi/2$
3	$\pi/2$	0	d_3	θ_3

Extended Data Table 2 | The robot's velocities and COTs for all gaits

Gait	Velocity (m/s, bl/s)	CoT
Paddling	0.0655 m/s (0.20 bl/s)	4.3
Best flapping	0.0833 m/s (0.26 bl/s)	3
Creep (porcelain)	0.0290 m/s (0.09 bl/s)	10.6
Creep (concrete)	0.0197 m/s (0.062 bl/s)	15.5
Creep (granite)	0.0141 m/s (0.044 bl/s)	21
Crawl (porcelain)	0.0301 m/s (0.094 bl/s)	15.3
Crawl (intertidal)	0.0186 m/s (0.058 bl/s)	30
Crawl (sand)	0.0246 m/s (0.077 bl/s)	17.8

Extended Data Table 3 | Experimentally determined friction coefficients between ART's constituent materials and the various tested substrates

-	Porcelain	Sand	Intertidal
PLA	0.3251	0.5263	0.6854
Elastomer	1.0447	0.5345	0.4960
Bellows	0.355	0.5536	0.4540